Title	A multi-scale crystal plasticity model for cyclic plasticity and low-cycle fatigue in a precipitate-strengthened steel at elevated temperature
Author(s)	Li, Dong-Feng; Barrett, Richard A.; O'Donoghue, Padraic E.; O'Dowd, Noel P.; Leen, Sean B.
Publication Date	2016-12-24
Publication Information	Li, Dong-Feng, Barrett, Richard A., O'Donoghue, Padraic E., O'Dowd, Noel P., & Leen, Sean B. (2017). A multi-scale crystal plasticity model for cyclic plasticity and low-cycle fatigue in a precipitate-strengthened steel at elevated temperature. Journal of the Mechanics and Physics of Solids, 101, 44-62. doi: https://doi.org/10.1016/j.jmps.2016.12.010
Publisher	Elsevier
Link to publisher's version	https://doi.org/10.1016/j.jmps.2016.12.010
Item record	http://hdl.handle.net/10379/15642
DOI	http://dx.doi.org/10.1016/j.jmps.2016.12.010

Accepted by the Journal (DOI: 10.1016/j.jmps.2016.12.010)

A multi-scale crystal plasticity model for cyclic plasticity and low-cycle fatigue in a precipitate-strengthened steel at elevated temperature

Dong-Feng Li[a,b,*], Richard A. Barrett[b], Padraic E. O'Donoghue[c], Noel P. O'Dowd[d,1], Sean B. Leen[b,1]

[a] *Shenzhen Graduate School, Harbin Institute of Technology, Shenzhen 518055, China*
[b] *Mechanical Engineering, College of Engineering and Informatics, NUI Galway, Ireland*
[c] *Civil Engineering, College of Engineering and Informatics, NUI Galway, Ireland*
[d] *School of Engineering, Bernal Institute, University of Limerick, Limerick V94 T9PX, Ireland*

Abstract

In this paper, a multi-scale crystal plasticity model is presented for cyclic plasticity and low-cycle fatigue in a tempered martensite ferritic steel at elevated temperature. The model explicitly represents the geometry of grains, sub-grains and precipitates in the material, with strain gradient effects and kinematic hardening included in the crystal plasticity formulation. With the multiscale model, the cyclic behaviour at the sub-grain level is predicted with the effect of lath and precipitate sizes examined. A crystallographic, accumulated slip (strain) parameter, modulated by triaxiality, is implemented at the micro-scale, to predict crack initiation in precipitate-strengthened laths. The predicted numbers of cycles to crack initiation agree well with experimental data. A strong dependence on the precipitate size is demonstrated, indicating a detrimental effect of coarsening of precipitates on fatigue at elevated temperature.

Keywords: Tempered martensite ferritic steels; Strain gradient-based crystal plasticity; Cyclic softening fatigue; Finite element; Crack initiation

1. Introduction

Advances in the understanding of mechanisms of material degradation in cyclic plasticity and in relevant modelling techniques in the past decade have created opportunities for more explicit consideration of the role of microstructure in the formation of fatigue cracks in realistic structural components. Recent trends in structural integrity assessments aim to take these microstructural advances into account (Sangid, 2013; Dunne, 2014) leading to more accurate life prediction and optimised design for cyclically-loaded materials and structural components.

The present study focuses on P91 steel (X10CrMoVNb9-1), which contains 9% Cr, 1% Mo and the balance primarily Fe and is a widely used structural material for power plant components. As discussed by numerous researchers (e.g., Sawada et al., 2011; Fedorova

*Corresponding author. Phone: +86 (0)755 86146861 Fax: +86 (0)755 86146861
Email addresses: lidongfeng@hitsz.edu.cn (Dong-Feng Li), richard.barrett@nuigalway.ie (Richard A. Barrett), padraic.odonoghue@nuigalway.ie (Padraic E. O'Donoghue), noel.odowd@ul.ie (Noel P. O'Dowd), sean.leen@nuigalway.ie (Sean B. Leen)
[1] Joint senior author.

et al., 2013), P91 has a complex microstructure with a hierarchical arrangement of prior-austenite grains, packets and blocks generated during austenite-martensite transformation. A block can be treated as a bcc 'grain', with a unique crystallographic orientation. At the sub-grain level (within a block) the material exhibits a lath-precipitate microstructure, which includes laths slightly misoriented (separated by dislocations) and precipitates mainly located at lath boundaries (Sauzay et al., 2005). When operating at elevated temperature, the grain-level microstructure is generally stable, while the sub-grain microstructure evolves, leading to coarsening of laths and precipitates with associated material softening (Sauzay et al., 2005; Srinivas Prasad et al., 2012; Fedorova et al., 2013; Hu et al., 2014). Under the operating conditions of flexible power plants, the relevant components typically experience both creep and fatigue loads. There is a practical need to examine the effect of lath and precipitate coarsening, during creep, on fatigue behaviour (creep-fatigue interaction) in order to comprehensively understand the mechanisms of premature failure. The present work examines the cyclic failure response of P91 at elevated temperature, focusing on the role of microstructure evolution on crack initiation. Sauzay et al. (2005) and Hu et al. (2014) have shown, based on microscopy characterisation, that considerable cyclic softening occurs along with microstructural recovery at the sub-grain level, in terms of coarsening of laths and precipitates under low cycle fatigue (LCF) conditions. In addition, fatigue damage, in terms of crack initiation and propagation, has also been observed in P91 steels under high temperature LCF conditions (Okamura et al., 1999). It has been found in these studies that multiple surface cracks are formed in the early stages of LCF cycles (approximately 10–20% of fatigue life) and may further contribute to cyclic softening. Indeed, multiple cracking and coalescence can commonly occur in LCF tests, as indicated by McDowell and Dunne (2010). Overall, recovery and damage are thus believed to be the two most important mechanisms responsible for cyclic softening in P91 steels at elevated temperature and both aspects will be examined in this work. Since P91 steels typically exhibit a non-saturated cyclic softening response, it is difficult to distinguish the active regimes of the individual softening mechanisms by means of the saturated-stress method (Sweeney et al., 2014).

The mechanism of fatigue for metals is the formation and development of persistent slip bands (PSB) during cyclic inelastic deformation (Sangid, 2013). In recent decades, microstructure-based simulations have been developed to understand and quantify the fatigue response in metals. In these models, the constitutive response at the microscale relies typically upon crystal plasticity theory, which is typically implemented within finite element (FE) tools (Roters et al., 2010). Length-scale dependence has been successfully incorporated into crystal plasticity FE (CPFE) models to account for strain gradient effects such that local deformation at the grain level can be accurately simulated and predicted (e.g., Busso et al., 2000; Dunne et al., 2012). For P91 steels at room temperature, strain gradient crystal plasticity FE modelling has been carried out to investigate multiscale precipitate hardening behaviour (Li et al., 2014a). Furthermore, numerical simulations have been applied to metallic materials along with the concept of fatigue indicator parameters (FIPs) as illustrated by Sangid (2013) and Dunne (2014), such as plastic strain based indicators (Dunne et al., 2007; Sweeney et al., 2013), the crystallographic work parameter (Sweeney et al., 2014) and non-local failure criteria (Anahid et al., 2011). In addition, crystal plasticity modelling based on real 3D EBSD microstructures for predicting fatigue crack location has been carried out by Signor et al. (2016), who found that the grain with observed fatigue cracking experiences the most intense accumulated plastic slip. The accumulated plastic slip has also been used by Maitournam et al. (2011), to predict high cycle fatigue crack initiation, albeit with the macroscale and mesoscale connected through homogenisation, rather than microstructure based finite element

simulation. Models (LE et al., 2015; Pessard et al., 2012; Morel and Huyen, 2008) accounting for anisotropic high cycle fatigue associated with defects have also been developed based on the fatigue criterion of accumulated plastic slip. However, microstructure-sensitive modelling of fatigue crack initiation (FCI) in P91 steels has not yet been studied. LCF micromechanical modelling of P91 steels at elevated temperature requires particular consideration of the localised cyclic plasticity and fatigue behaviour. A key objective in the LCF modelling of P91 steels, therefore, is to spatially predict the evolution of cyclic micro-strains and hence fatigue crack initiation to understand the roles of laths and precipitates specifically.

The objectives of the current paper are as follows: (i) Develop multiscale finite-element models to explicitly represent the geometry of grains, sub-grains and precipitates with strain gradient effects and kinematic hardening included in the crystal plasticity formulation; (ii) Examine the microstructure-sensitive cyclic behaviour, in terms of sites and number of cycles to critical levels of crystallographic slip (strain) for crack initiation, using the multiscale model and compare predictions with experiments; (iii) Analyze LCF test data for P91 steels at elevated temperature to estimate cyclic softening and hence the number of cycles to crack initiation. The primary novel aspect of this work, compared to our recent work (Li et al., 2014a, 2016), is the representation of length-scale effects for high temperature, cyclic plasticity of the lath-precipitate (micro-scale) microstructural unit, using a dislocation mechanics formulation for annihilation and accumulation of dislocation density evolution. Previous work by the authors on the lath-precipitate (micro-scale) microstructural unit was limited to monotonic, room temperature behaviour (Li et al., 2014a). In addition to this, a top-down multiscale connection method is used in the current work rather than the bottom-up one in the previous work such that the fatigue crack initiation life can be accurately predicted. Li et al. (2016) has recently presented cyclic plasticity and fatigue modelling results for meso-scale thermo-mechanical fatigue behaviour. However, that work did not predict lath-precipitate response, which is the key focus of the present multi-scale methodology.

2. High temperature cyclic softening and fatigue crack initiation of P91

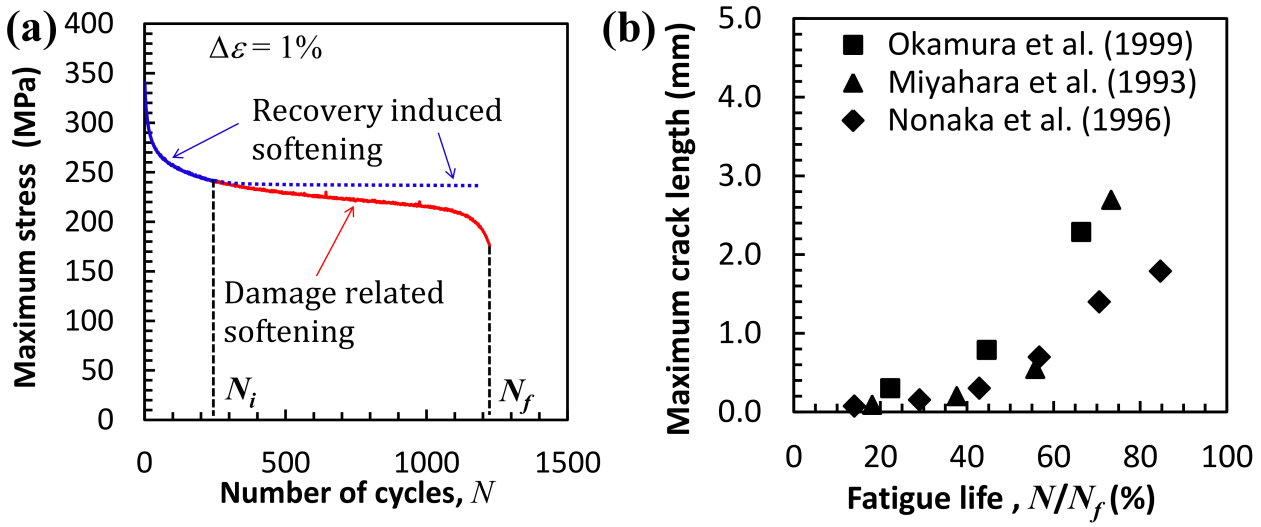

Figure 1: Typical LCF data with (a) cyclic softening of P91 steels at 600° C with $\triangle\varepsilon = 1\%$, where N_i and N_f illustratively indicate the number of cycles to fatigue crack initiation and fatigue failure, respectively and (b) measured surface crack length at different stages of LCF lifes.

In order to investigate the high temperature fatigue behaviour for ex-service P91 steel (with 35,168 h of service), Farragher (2014) has carried out fully reversed strain-controlled cyclic tests at 600° C at a constant strain rate of $3.3 \times 10^{-4}\ s^{-1}$. Figure 1a shows the maximum stress vs the number of cycles in a typical test ($\triangle\varepsilon = 1\%$). In this work, it is assumed that the softening response can be divided into an initial recovery phase and a more gradual damage phase. Considerable cyclic softening (reduction of maximum stress) can be seen in the figure. When $N < N_i$, cyclic softening is induced by high temperature recovery in terms of dislocation annihilation and microstructure coarsening, which reduces the dislocation density in the material. When $N > N_i$, micro-crack nucleation, coalescence and macro-crack propagation inevitably occur leading to macro-degradation and rapid failure at $N = N_f$. For P91 steel at 600° C, numerous experimental studies (e.g., Okamura et al., 1999) have shown that multiple surface fatigue cracks form at the early stage of fatigue life, $N/N_f \approx 10 - 20\%$. Figure 1b shows the data of maximum surface crack length at different N/N_f. In order to estimate N_i from the test data, a theoretical method is presented to analyse the recovery-induced cyclic softening in this paper. The details of the method are given in the appendix.

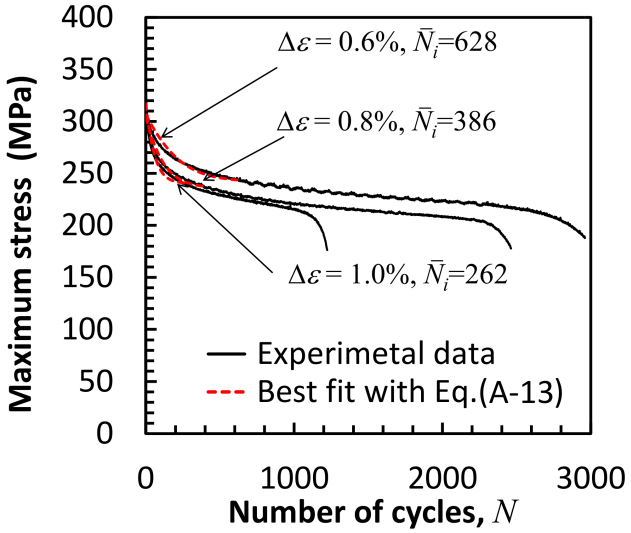

Figure 2: Identification of N_i in LCF tests of P91 steel at 600° C with the best fits from the theoretical solution to the experimental data (Farragher, 2014) (these fits have identical correlation index, $R^2 = 0.95$).

In Fig. 2, $\bar{N}_i$ represents the identified value of N_i. The approximate method presented here infers a crack nucleation life from the measured softening curves, based on the evolution of dislocation density from a Kocks-Mecking type model, by demarcating the transition from recovery-induced softening to fatigue damage induced softening. This inferred crack initiation life, based on the measured softening curves, is used to compare against the multi-scale predictions (Section 4.3).

The present paper focuses on the fatigue behaviour of P91 steel at 600° C. In order to characterise the fatigue mechanisms, SEM-based fractographic analysis has been performed with the following figure showing the fracture surface after HT fatigue. In Fig. 3a, both fatigue striations and voids (different sizes) can be clearly identified. The voids in HT fatigue are attributed in origin to thermally-induced decohesion from secondary precipitates and to grain boundary cavitation, as described by Suresh (1998). The identified voids with different sizes are evidence of void growth during HT fatigue. Smaller scale experimental observations of the high temperature, cyclic deformation crack nucleation phase is desirable, even if this has not

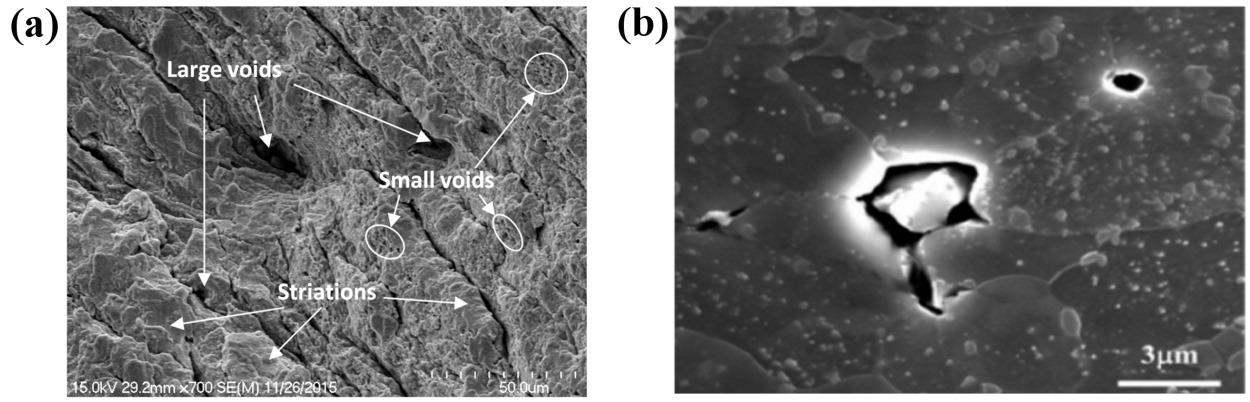

Figure 3: Experimental observations of voids in P91 with (a) microscopy of the failure surface after high temperature fatigue for the present P91 steel and (b) void nucleation and coalescence in P91 crept at 600° C (which is adapted from Lee and Murayama, 2015).

yet been achievable. Of relevance here is the recent work of Lee and Murayama (2015), who present microscopy observations of nano-void nucleation at carbide precipitates, as well as nano-void coalescence in P91, as in Fig. 3b, at similar temperature conditions to the present work. In addition, the X-ray tomography method (e.g. Terzi et al., 2009; Grogan et al., 2015) has also shown capability to capture in-situ the void nucleation and evolution.

3. Multiscale finite element modelling for cyclic plasticity and low cycle fatigue

3.1. Implementation of microstructure-sensitive multiscale finite element models

In the present work, a microstructure-sensitive multiscale FE modelling methodology is developed to predict the effects of key variables on cyclic plasticity and LCF crack initiation for P91 steels at 600° C. Figure 4 shows the material microstructure and the use of FE modelling at both the grain and sub-grain levels. In order to monitor the mechanical response at the macroscopic level, a microstructure map obtained by EBSD, as shown in Fig. 4b, has been used to implement a polycrystal FE model (Fig. 4d), in which geometrical details of measured blocks are incorporated. The scanned region of EBSD has a dimension of 176 $\times$ 111 μm^2, which is identical to the size of the polycrystal FE model. As indicated by Li et al. (2014a), a representative and stable result, in terms of macroscopic stress strain response, can be achieved using such microstructure-based FE models. In Fig. 4b, crystallographic orientations of different grains are distinguished by an inverse pole map. The Euler angles (Li and O'Dowd, 2011) are used to represent crystallographic orientations in the polycrystal FE model (Fig. 4d shows the field plot of the second Euler angle). The FE representation of Fig. 4d has been compared with the EBSD map of Fig. 4b, to identify individual blocks in both images. Examples of these are highlighted by black borders, as labelled 1, 2, 3 and 4, in both images. These demonstrate that the Euler angle representation of Fig. 4d is consistent with the EBSD map of Fig. 4b. The FE model uses regular 3D brick elements (8 nodes and cubic shape with edge length of 0.5 μm) and is constrained by periodic boundary conditions in both in-plane and out-of-plane directions. This polycrystal FE model is considered suitable to capture the most relevant in-plane grain interactions when in-plane uniaxial loading is applied. The strain gradient crystal plasticity model discussed in Section 3.2 is then used to represent the constitutive response of each single crystal (block). In order to examine the potential variability in the crack initiation prediction, another EBSD microstructure with

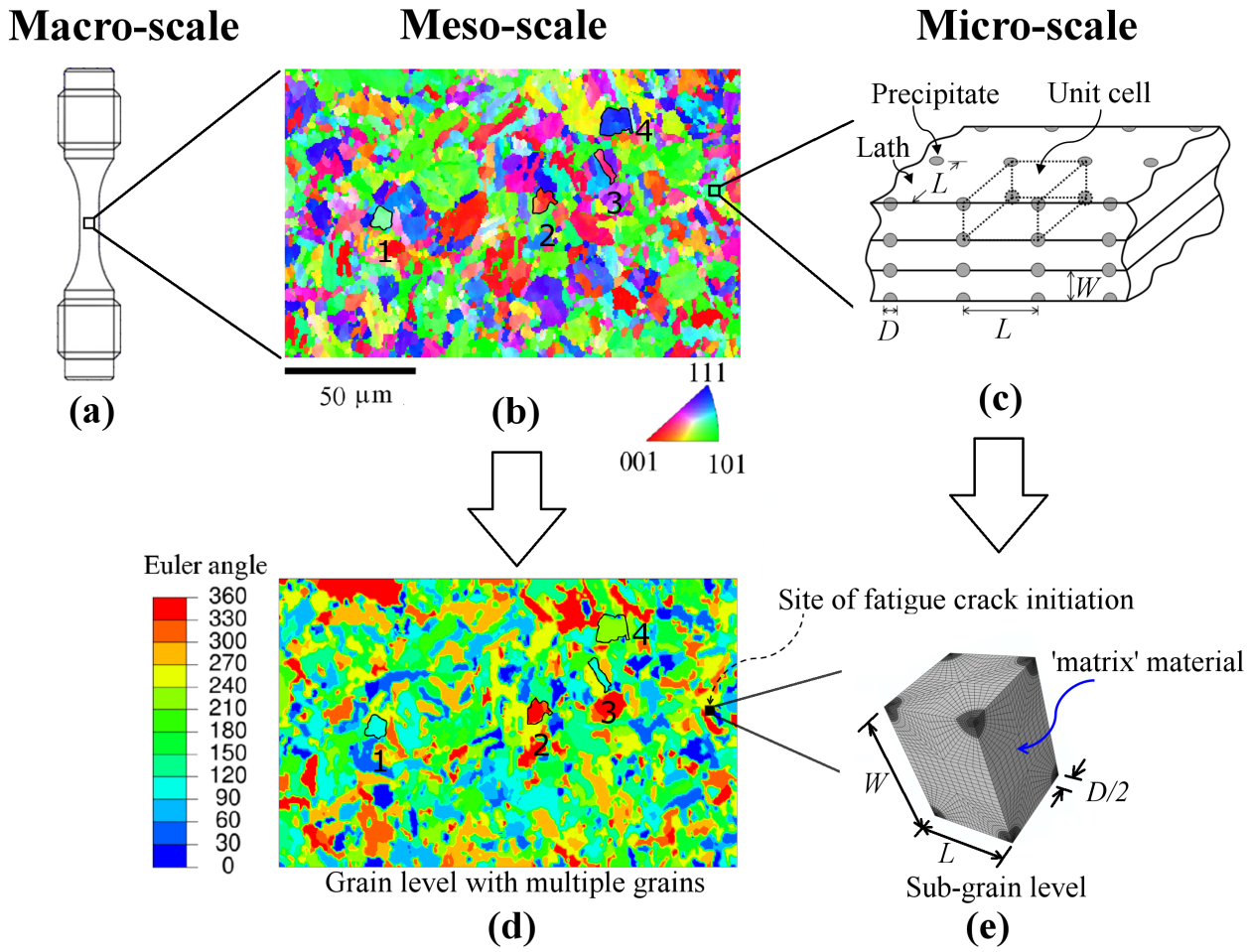

Figure 4: Multiscale finite element modelling methodology for fatigue crack initiation in P91 steels with (a) illustration of low cycle fatigue specimen; (b) microstructure morphology measured by EBSD including sample highlighted blocks 1 to 4; (c) illustration of lath-precipitate microstructure at the sub-grain level; (d) the spatial distribution of Euler angle in a polycrystal finite element model including sample highlighted blocks 1 to 4; and (e) the unit-cell finite element model at the sub-grain level.

identical dimensions to that of Fig. 4b has also been examined. The grain (block) boundary identified by electron backscatter diffraction (EBSD) is piece-wise linear rather than smooth as a result of pixel scan. In order to reflect these measurements, the current model uses an identical piece-wise grain boundary to match the EBSD measurement. However, note that a very fine mesh is used for the analysis, so a typical finite element length is 0.5 μm, with typically 10 elements along a grain (block) boundary. The methodology adopted here has been successfully validated, including detailed mesh and RVE convergence studies for room temperature monotonic behaviour (Li et al., 2014a). Ongoing work is focused on the detailed effects of grain boundary representations (e.g. using higher order interpolation) on GND evolution and hence on fatigue crack nucleation.

Figure 4c shows a schematic of the sub-grain structure of P91, where the most relevant precipitates, $M_{23}C_6$ carbides with a size range of approximately 100–460 nm (Srinivas Prasad et al., 2012; Fedorova et al., 2013), are located on lath boundaries, and are represented as regularly arranged spherical precipitates. The 3D FE model is shown in Fig. 4e, with periodic boundary conditions applied. The lath unit cell model is subjected to the local multiaxial

strain-controlled loading history, corresponding to the local response at the relevant location in the meso-scale model of Fig. 4d, implemented via displacement control of the faces. This FE mesh has been shown to ensure convergence of results with regard to mesh sensitivity (Li et al., 2014a). The strain gradient effects are strongest in the sub-micron lath model because the smallest microstructural features are the precipitates. A misorientation angle (2.5° on average) exists between neighbouring laths, which is incorporated here through the use of geometrically necessary dislocations (Li et al., 2014a). As discussed in the work of Li et al. (2014a), the small angular misorientation between neighbouring laths has a negligible effect on the mechanical response and on the resultant strain gradient compared to the influence of the precipitates. This was established through an analysis with an extended RVE containing more than one lath with a misorientation angle of 2.5 degrees, demonstrating a negligible difference in the overall stress-strain response and the local accumulated plastic strain. The orientation of the micro-scale (lath) crystal of Fig. 4e is that of the specific (critical) site in the meso-scale model, which it represents. The precipitate response is assumed to be elastic with identical anisotropic constants to P91, while the surrounding 'matrix' material may deform plastically (Li et al., 2014a). The volume fraction (V_f) of carbide precipitates is 1.9% (Srinivas Prasad et al., 2012), which is assumed to remain unchanged during the high temperature cyclic plasticity test. As shown in Fig. 4c, the unit-cell FE model has three geometrical parameters, precipitate diameter, D, lath thickness, W, and precipitate spacing, L. Only two are independent (D and W are chosen in the current work). Note that the present lath model focuses primarily on the $M_{23}C_6$ precipitates, although other types of precipitates may also exist, e.g. MX carbonitrides, which disperse in the matrix material having relatively small size (10–90 nm) and volume fraction (0.1–0.6%) (e.g., Srinivas Prasad et al., 2012; Fedorova et al., 2013).

3.2. Crystal plasticity-based constitutive formulation

3.2.1. Constitutive response at the block level

The length-scale dependent crystal plasticity model presented by Li et al. (2014a) for P91 steels has been extended to include non-linear kinematic hardening in order to correctly represent the cyclic response of the material. Although the focus of the present work is on macro-scale strain ranges of less than 1%, non-linear kinematics has been employed to describe the finite deformation and rotations at the local (meso- and micro-scales) level. Furthermore, a dislocation density-based crystal plasticity model has been used for P91 steel to represent the physical cyclic softening mechanisms and the length-scale dependence. The deformation gradient, $\mathbf{F}$, is represented by a multiplicative decomposition:

$$\mathbf{F} = \mathbf{F}^e\mathbf{F}^p, \tag{1}$$

where $\mathbf{F}^e$ and $\mathbf{F}^p$ denote the elastic and plastic parts of $\mathbf{F}$, respectively. The elastic material model is assumed to be linear as the magnitude of elastic deformation is much smaller than that of plastic deformation. The inelastic deformation occurs in terms of the crystallographic slip on twelve $\langle 111\rangle\{110\}$ slip systems. As shown by Franciosi et al. (2015) and also in the work of Ali et al. (2011) and Marichal et al. (2013), for bcc metals $\langle 111\rangle$ is the slip direction and the $\{110\}$ slip planes are the primary slip planes. In addition, there is no retained austenite in the P91 steels, which can be confirmed by our recent neutron diffraction measurement (Li et al., 2014b) and the synchrotron pattern of Wang et al. (2014). Therefore, for computational efficiency (bearing in mind the large numbers of blocks and sub-grains in the meso- and micro-scale models), the present model assumes that slip occurs only on $\{110\}$ planes. The plastic

deformation rate is related to the crystallographic slip rate,

$$\mathbf{L}^p = \dot{\mathbf{F}}^p \left(\mathbf{F}^p\right)^{-1} = \sum_{\alpha=1}^{M} \dot{\gamma}^\alpha \mathbf{m}^\alpha \otimes \mathbf{n}^\alpha, \tag{2}$$

where $\dot{\gamma}^\alpha$, $\mathbf{m}^\alpha$ and $\mathbf{n}^\alpha$ are the slip rate, slip direction and slip plane normal of the slip system, α, respectively, M refers to the total number of slip systems (M is equal to 12 in this paper) and $\otimes$ indicates a dyadic product. In the current work, a thermally activated flow rule developed by Busso and McClintock (1996), with slip rate $\dot{\gamma}^\alpha$ as a function of resolved shear stress τ^α and slip resistance S^α, is adopted as follows

$$\dot{\gamma}^\alpha = \dot{\gamma}_0 \exp\left\{-\frac{F}{k\theta}\left\langle 1 - \left\langle \frac{|\tau^\alpha - B^\alpha| - S^\alpha}{\tau_0} \right\rangle^{q_1} \right\rangle^{q_2}\right\} \operatorname{sgn}\left(\tau^\alpha - B^\alpha\right), \tag{3}$$

where F, k and θ are the Helmholtz free energy for a material, Boltzmann constant and absolute temperature, respectively; q_1, q_2 and $\dot{\gamma}_0$ are the exponents and pre-exponential constants; τ_0 is the critical shear stress associated with the overall forest dislocations, which is the shear stress required to cut through the material on the slip plane (Ma et al., 2006); the brackets $\langle . \rangle$ indicate that $\langle x \rangle \equiv x$ for $x > 0$ and $\langle x \rangle \equiv 0$ for $x \leq 0$; B^α and S^α are back stress and slip resistance for the slip system, α, respectively.

The evolution of the back stress, B^α, follows an Armstrong-Frederick type kinematic hardening rule (e.g., Busso and McClintock, 1996),

$$\dot{B}^\alpha = h_b \dot{\gamma}^\alpha - \frac{r_D}{S^\alpha} B^\alpha |\dot{\gamma}^\alpha|, \tag{4}$$

where h_b and r_D are material constants. The physical basis of Eq. (4) with regard to the interaction between dislocations and precipitates has been discussed by Busso and McClintock (1996). Comparing to our previous work (Li et al., 2014a), the back stress evolution equation is a new term which accounts for the kinematic hardening of P91. As in the work of Li et al. (2014a), slip resistance is given by

$$S^\alpha = \mu b \sqrt{\sum_{\beta=1}^{M} h_0 \left[\omega_1 + (1 - \omega_2)\, \delta^{\alpha\beta}\right] \left(\rho_{Se}^\beta + \rho_{Ss}^\beta + \rho_G^\beta\right)}, \tag{5}$$

where μ and b are the shear modulus and the magnitude of the Burgers vector, respectively; ρ_{Se}^β, ρ_{Ss}^β and ρ_G^β are the edge part of statistically stored dislocation (SSD) density, the screw part of SSD density and the geometrically necessary dislocation (GND) density for the slip system β, respectively; h_0 is a coefficient indicating the strength of dislocation pair interactions; ω_1 and ω_2 are interaction constants and $\delta^{\alpha\beta}$ is the Kronecker delta. In the present work, it is assumed that all dislocations interact equally, which leads to $\omega_1 = \omega_2 = 1$.

Following Li et al. (2014a), the critical shear stress, τ_0, depends on dislocation density as follows

$$\tau_0 = \hat{\tau}_0 + c_\tau \sqrt{\sum_{\beta=1}^{M} \left(\rho_{Se}^\beta + \rho_{Ss}^\beta + \rho_G^\beta\right)}, \tag{6}$$

where $\hat{\tau}_0$ is the critical shear stress in the absence of dislocation barriers and c_τ is a coefficient for dislocation densities which may be obtained from dislocation dynamics simulations. As

shown by Cheong and Busso (2006), the rates of ρ^{α}_{Se} and ρ^{α}_{Ss} on each slip system are as follows

$$\dot{\rho}^{\alpha}_{Se} = \left[\frac{K_e}{b} \sqrt{\sum_{\beta=1}^{M} \left(\rho^{\beta}_{Se} + \rho^{\beta}_{Ss} + \rho^{\beta}_{G} \right)} - d_e \rho^{\alpha}_{Se} \right] |\dot{\gamma}^{\alpha}|, \tag{7a}$$

$$\dot{\rho}^{\alpha}_{Ss} = \left[\frac{K_s}{b} (1 - \frac{\pi d_s^2}{4} \rho^{\alpha}_{Ss}) \sqrt{\sum_{\beta=1}^{M} \left(\rho^{\beta}_{Se} + \rho^{\beta}_{Ss} + \rho^{\beta}_{G} \right)} - d_s \rho^{\alpha}_{Ss} \right] |\dot{\gamma}^{\alpha}|, \tag{7b}$$

where K_e and K_s are two coefficients of dislocation generation for the slip system α, and d_e and d_s are two coefficients relating to the annihilation of edge and screw dislocations, respectively. In this work, it is assumed that $K_s = 2K_e$ based on the work of Cheong and Busso (2006).

The GND density, ρ^{α}_{G}, is written as a sum of three parts,

$$\rho^{\alpha}_{G} = |\rho^{\alpha}_{Gsm}| + |\rho^{\alpha}_{Get}| + |\rho^{\alpha}_{Gen}|, \tag{8}$$

where ρ^{α}_{Gsm} is the pure screw component in the slip direction, $\mathbf{m}^{\alpha}$, and ρ^{α}_{Get} and ρ^{α}_{Gen} are the pure edge components in the directions, $\mathbf{t}^{\alpha}$ ($\mathbf{t}^{\alpha} = \mathbf{n}^{\alpha} \times \mathbf{m}^{\alpha}$) and $\mathbf{n}^{\alpha}$, respectively. Based on the work of Busso et al. (2000), the GND densities evolve as follows

$$\dot{\rho}^{\alpha}_{Gsm} \mathbf{m}^{\alpha} + \dot{\rho}^{\alpha}_{Get} \mathbf{t}^{\alpha} + \dot{\rho}^{\alpha}_{Gen} \mathbf{n}^{\alpha} = \frac{1}{b} \mathrm{curl} \left(\dot{\gamma}^{\alpha} \mathbf{n}^{\alpha} \mathbf{F}^{p} \right). \tag{9}$$

The term on the right hand side of Eq. (9) defines an equivalent GND density rate vector for the slip system, α. With respect to contributions of different parts of GND density to slip resistance, the slip resistance depends on the total dislocation density (Eq. 5), which is defined as a sum of edge and screw parts of dislocation density (Eq. 8). Edge and screw dislocations can lead to distinct dynamic recovery processes (e.g., Cheong and Busso, 2004), and make different contributions to the formation of sub-grain structures, e.g., persistent slip bands (e.g., Essmann and Mughrabi, 1979). Hence, the evolving processes are quantitatively accounted for here with different equations (Eqs. 7a and b) introduced for the two dislocation densities.

The accumulated equivalent plastic slip (strain), representing an average (over all slip systems) measure of local accumulated crystallographic micro-strain or micro-slip, is defined here by

$$\bar{\varepsilon}_p = \int_0^t \left(\frac{2}{3} \mathbf{D}^p : \mathbf{D}^p \right)^{\frac{1}{2}} d\tau, \tag{10}$$

where t is the current time, τ is integration variable and $\mathbf{D}^p$ is plastic strain rate defined as

$$\mathbf{D}^p = \frac{1}{2} \sum_{\alpha=1}^{12} \dot{\gamma}^{\alpha} \left[\mathbf{F}^e \mathbf{m}^{\alpha} \otimes \mathbf{n}^{\alpha} \left(\mathbf{F}^e \right)^{-1} + \left(\mathbf{F}^e \right)^{-T} \mathbf{n}^{\alpha} \otimes \mathbf{m}^{\alpha} \left(\mathbf{F}^e \right)^{T} \right]. \tag{11}$$

In order to compute the strain gradient term on the right hand side of Eq. (9), a user element subroutine (UEL) has been implemented within a commercial FE code, ABAQUS (2011), with the evolution of GND densities and the length scale dependency accounted for. The element type used in the UEL is an 8-node, 3D continuum element with linear shape functions. Further details of the original UEL formulation, which is modified here, can be found in the work of Busso et al. (2000) and Li et al. (2014a).

3.2.2. Response at the sub-grain (lath) level

The strain gradient crystal plasticity model described in the previous section is also used to represent the response of the lath 'matrix' (Fig. 4e). However, kinematic hardening is not included in the constitutive model at the sub-grain level as the hardening mechanism is incorporated explicitly through the inclusion of precipitates within the plastically deforming matrix (Kassner et al., 2009) leading to back stresses during cyclic deformation. Thus $B^{\alpha} = 0$ in the flow rule, Eq. (3) for the lath 'matrix' (alternatively, $h_b = r_D = 0$ in Eq. 4). All other material parameters for the matrix are assigned the same values as at the block level (Fig. 4d). Since attention is focused on isothermal behaviour of P91 steels at 600° C, the present work does not involve a thermal step to consider the internal stress attributed to inhomogeneous thermal expansions of different phases, e.g., the matrix and precipitates of the micro-scale lath model. The material presented for the meso-scale model is a single-phase material.

3.3. Fatigue indicator parameter at the nano-scale

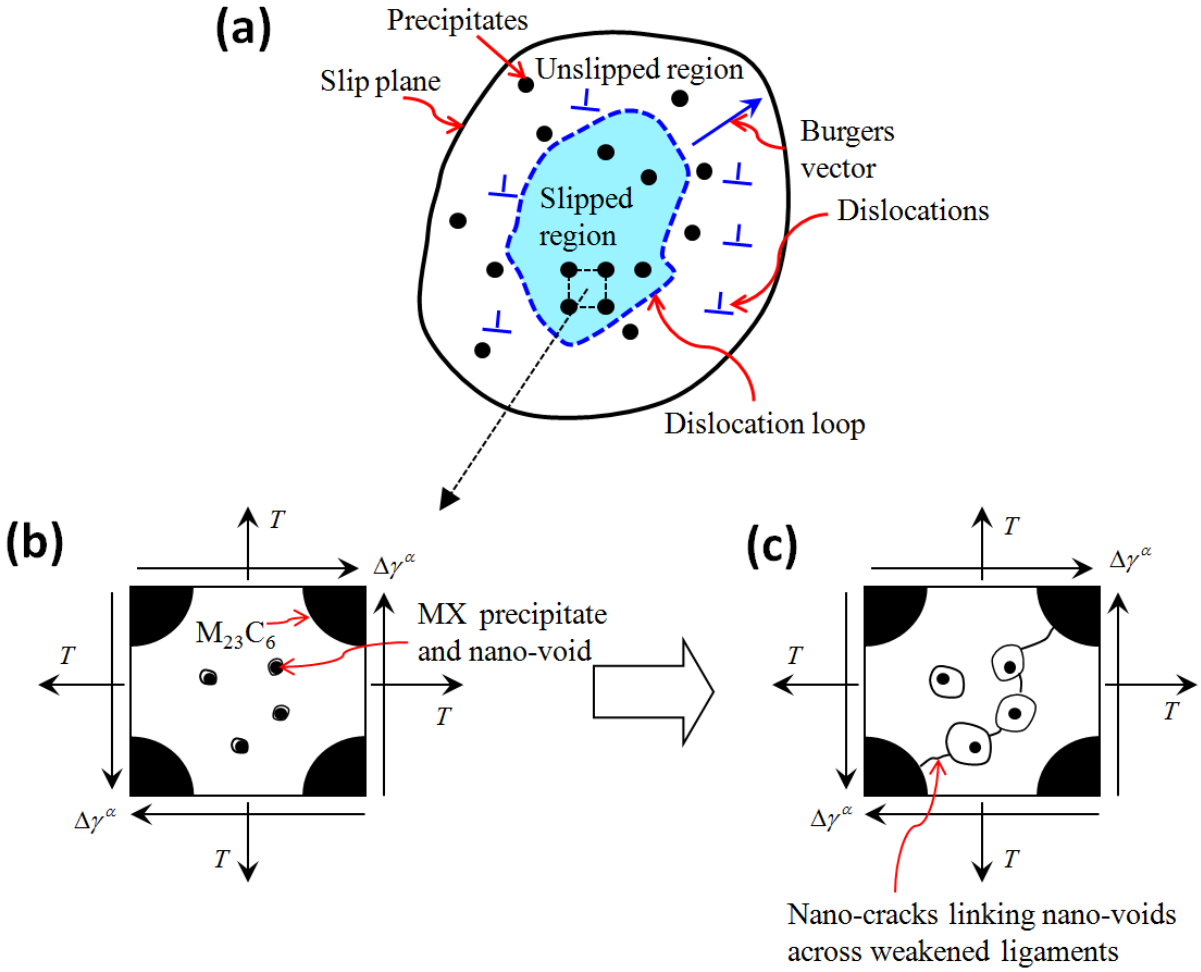

Figure 5: Schematics of the postulated fatigue crack initiation mechanisms with (a) the illustrative arrangement of dislocations and precipitates on the slip plane; (b) the nano-void nucleation and (c) the nano-void growth and nano-cracking, where the lath unit is subject to stress triaxility, T, and incremental crystallographic shear slip, $\Delta\gamma^{\alpha}$.

The mechanism on which the FCI model is predicated is localised, cyclic accumulation of plastic deformation via crystallographic slip, causing gradual material degradation via nano-void nucleation, growth and coalescence and, hence nano-crack propagation for LCF (e.g.

Kuwamura, 1997; Rosien and Ostertag, 2009; Mughrabi , 2013). In the present work for L-CF, physically, such nano-voids can initiate in the matrix material as a result of dispersed second-phase particles, e.g., MX precipitates which are typically less than 50 nm. Fig. 5 shows the FCI mechanism proposed to be modelled in the present work. Here, Fig. 5a presents the arrangement of the dislocations and precipitates on the slip plane, which have been explicitly accounted for in the present work. Figs. 5b and c illustrate the nano-void nucleation (attributed, for example, to MX precipitate-matrix decohesion, due to localised crystallographic slip concentration) and growth, respectively, which have been taken into account in the present work through the use of lath-precipitate model along with a specific fatigue criterion, as shown below.

FCI is deemed to occur when a critical value of local accumulated crystallographic slip is achieved in the unit-cell FE model (Fig. 4e). This is designated as a fatigue indication parameter (FIP). A similar approach has been adopted by Dunne et al. (2007) and more recently by Sweeney et al. (2013). Under multiaxial loading, we expect that FCI will have an additional dependence on the local stress state (triaxiality) as the limiting micro-slip will depend strongly on triaxiality. In order to account for this, the FIP calculated in the crystal plasticity model is modified by a triaxiality term. A similar approach has been used to account for the influence of stress triaxiality within a crystal plasticity based modelling framework for cyclic loading of titanium by Anahid et al. (2011). In the work of Kiran and Khandelwal (2015), a similar term has also been used in the computational study for low cycle fatigue (less than 100 cycles). Here, the accumulated crystallographic slip (strain), $\widetilde{\varepsilon}_p$, is defined as follows

$$\widetilde{\varepsilon}_p\left(N\right) = \sum_{n=1}^{N} \int_{t_n}^{t_{n+1}} \left(\frac{2}{3}\mathbf{D}^p : \mathbf{D}^p\right)^{\frac{1}{2}} \exp\left(kT - \frac{k}{3}\right) dt, \tag{12}$$

where t_n and t_{n+1} represent the start time of the n^{th} and $n+1^{\text{th}}$ cycle, respectively; $T = \frac{\sigma_m}{\sigma_{eq}}$, is the stress triaxiality; $\sigma_m = \frac{1}{3}\text{tr}\boldsymbol{\sigma}$ is hydrostatic stress for the Cauchy stress tensor, $\boldsymbol{\sigma}$; σ_{eq} is von Mises equivalent for the Cauchy stress tensor, $\boldsymbol{\sigma}$; k is a coefficient, which can be related to void geometry and material. Note that when $k = 0$, the effect of triaxiality, average micro-scale loading level, is switched off and the critical cyclic micro-slip is assumed to be independent of stress states. It should be noted that Trattnig et al. (2008) proposed a similar equation for macroscopic ductile failure of austenitic steels and $k = 1.88$ is suggested based on their experiments. In the present work, $k = 1.5$ has been used, as in the work of Anahid et al. (2011) and Kiran and Khandelwal (2015). Note here that as indicated by Mbiakop et al. (2015a) the initial void shape can affect void growth and coalescence; P91 material typically initiates sphere-shaped voids from the second phase spherical precipitates (Fig. 3b).

The fatigue crack initiation criterion is then given by

$$\widetilde{\varepsilon}_{crit} = \widetilde{\varepsilon}_p^{max}\left(N_i\right), \tag{13}$$

where $\widetilde{\varepsilon}_{crit}$ is a material constant representing micro-strain or micro-slip at the onset of nano-cracking, $\widetilde{\varepsilon}_p^{max}$ is the maximum value of $\widetilde{\varepsilon}_p$ in the model, N_i is the number of cycles to FCI. $\widetilde{\varepsilon}_p^{max}$ is computed in a non-local sense, averaged over all integration points within each element. The material constant, $\widetilde{\varepsilon}_{crit}$ can be identified by comparing the CPFE predicted $\widetilde{\varepsilon}_p^{max}$ from one test condition to the experimental value of N_i. The N_i for other LCF loading conditions (e.g. other tests, real applications) can then be predicted using the CPFE micro-model with Eq. (13). Note that in the current modelling work, the FIP is applied principally on the

micro-scale FE model (lath level), but can also be used on the meso-scale FE model at the block level (Li et al., 2016).

In the present work, the nano-voids are not explicitly included and more accurate quantifications with respect to nano-void geometries could be achieved by explicitly introducing them (similar to Brünig et al., 2013) into the FE model at the lath level. This will be examined in future work.

4. Results

4.1. Identification of constitutive material parameters

Table 1: Material parameters used in the polycrystal FE model for P91 steels at 600° C .

Elastic constants and flow parameters			Hardening parameters		
Parameter	Dimension	Value	Parameter	Dimension	Value
C_{11}	GPa	186.7	b	nm	0.251
C_{12}	GPa	126.3	h_0	–	0.014
C_{44} (or μ)	GPa	90.2	w_1	–	1.0
$\dot{\gamma}_0$	s^{-1}	10^6	w_2	–	1.0
q_1	–	0.5	K_e	–	2500
q_2	–	1.25	d_e	–	50
F	J	44.8×10^{-20}	d_s	–	250
$\hat{\tau}_0$	MPa	490[a]	h_b	MPa	5800
c_τ	N/mm	0.0027	r_D	MPa	200
ρ_0	$10^8 mm^{-2}$	4.2[b]			

[a] A value of 420 MPa is used for half-life.
[b] A value of 0.84 is used for half-life.

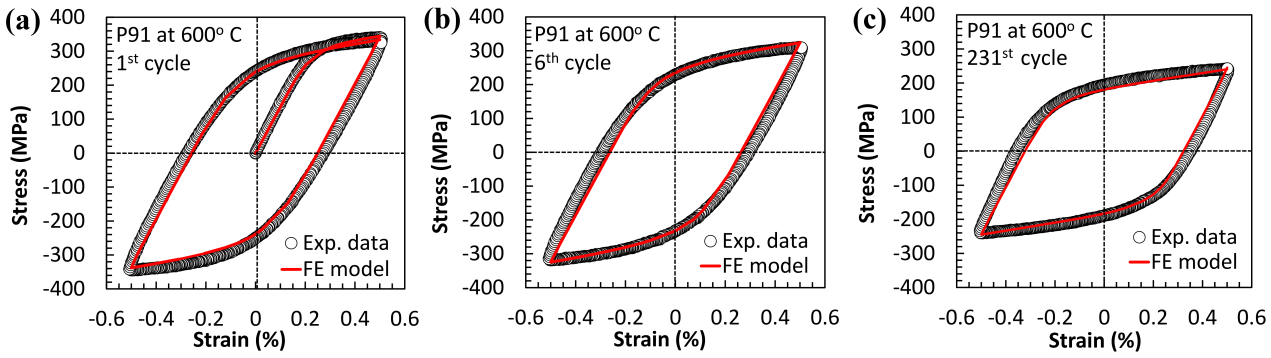

Figure 6: Comparison between the calibrated polycrystal FE model and experiment in terms of (a) the first hysteresis loop, (b) the sixth hysteresis loop and (c) the response representing the half-life hysteresis loop.

The crystal plasticity material model described in Section 3.2.1 relies on nineteen material parameters (including the three single crystal elastic constants). The current work is based on previous developments, including previously published identification and calibration against measured monotonic test data for P91 up to 600° C (Li et al., 2014a; Golden et al., 2015a). The validation of the polycrystal FE model for monotonic loading has been carried out using *in-situ* neutron diffraction measurement (Li et al., 2014b) and *ex-situ* EBSD measurement (Golden et al., 2015b) for room temperature behaviour. Table 1 gives the elastic

constants, flow parameters and the strain hardening parameters used in this work. Note that the present model extends the previous work (Li et al., 2014a) from room temperature and monotonic hardening to high temperature and cyclic hardening and a number of parameters are re-calibrated based on uniaxial cyclic test data at 600° C for the 1% strain range condition (Farragher, 2014). The high temperature single crystal elastic constants, C_{11}, C_{12} and C_{44} are based on the data in literature (e.g. Razumovskiy et al., 2011) and the measured macroscopic elastic response. The flow parameters, F, $\hat{\tau}_0$ and c_τ are adjusted to represent high temperature inelastic response and the other flow parameters are identical to those of Li et al. (2014a). For hardening parameters, the cross hardening parameters, w_0 and w_1 are unchanged, the magnitude of the Burgers vector is obtained according to the lattice parameter of bcc iron at 600° C, and the other parameters are identified based on the experimental hysteresis stress-strain loops. In addition, the identification of material parameters has also been carried out at temperatures of 400° C and 500° C for the same strain range, as shown in the work of Li et al. (2016) with elastic constants and h_b temperature dependent.

Figures 6a-c show the comparison between the simulated stress-strain hysteresis loops and the experimental data at 600° C for the first, sixth and half-life cycles. Very good agreement is achieved between modelling and experiment. Note that two measured microstructures have been simulated in order to examine computational scatter. The maximum stress difference between the two microstructural simulations is less than 3 MPa. The results of Fig. 6 are based on the microstructure given in Fig. 4d. The simulation of first six cycles uses the material parameters in Table 1 with slight cyclic softening predicted, which is consistent with experiment. In order to capture the significant long-term cyclic softening with a reduction of dislocation density typically observed, two parameters, initial dislocation density (ρ_0) and critical shear stress ($\hat{\tau}_0$), are allowed to evolve with values reduced. Here, we reduce the initial dislocation density and critical shear stress to one-fifth of the value for the initial six cycles and 420 MPa, respectively, to simulate long-term softening. The reduction ratio of ρ_0 is consistent with the experimental data by Sauzay et al. (2008) and Giroux (2011). The reduction of the critical shear stress is physically motivated by precipitate coarsening, based on Orowan strengthening mechanism (Orowan, 1948), which leads to increased precipitate spacing and hence decreased shear strength. No adjustments are applied on the internal variables, e.g., the back stress still evolves from zero. This approach has been shown to give consistently good correlation at the half-life for high temperature isothermal fatigue tests and thermo-mechanical fatigue tests by Li et al. (2016). Additional validation of the calibrated material model under cyclic loading for 0.6% and 0.8% strain-ranges is presented in the current paper in Section 4.2.1.

4.2. Calibration and validation of the meso- and micro-models

4.2.1. Analysis at the meso-scale

Figure 7 shows the comparison between the simulated and measured stress-strain responses for strain-controlled cyclic tests with applied strain ranges of 0.8% and 0.6%, as validation of the identified parameters of Section 4. In Figs. 7a-f, the predicted and measured hysteresis loops in the first, sixth and half-life cycles, for strain ranges of 0.8% and 0.6%, are compared. Very good agreement can be seen in the figures, with the combined (isotropic and kinematic) hardening of the material captured effectively by the polycrystal model. These simulations have also been carried out on two microstructures, as for the strain range of 1%. The results shown here are from the microstructure of Fig. 4d. There are only slight differences in the stress-strain response arising from the two microstructures. Comparing with the simulations at early cycles, significant cyclic softening is observed at the half-life number of cycles for both

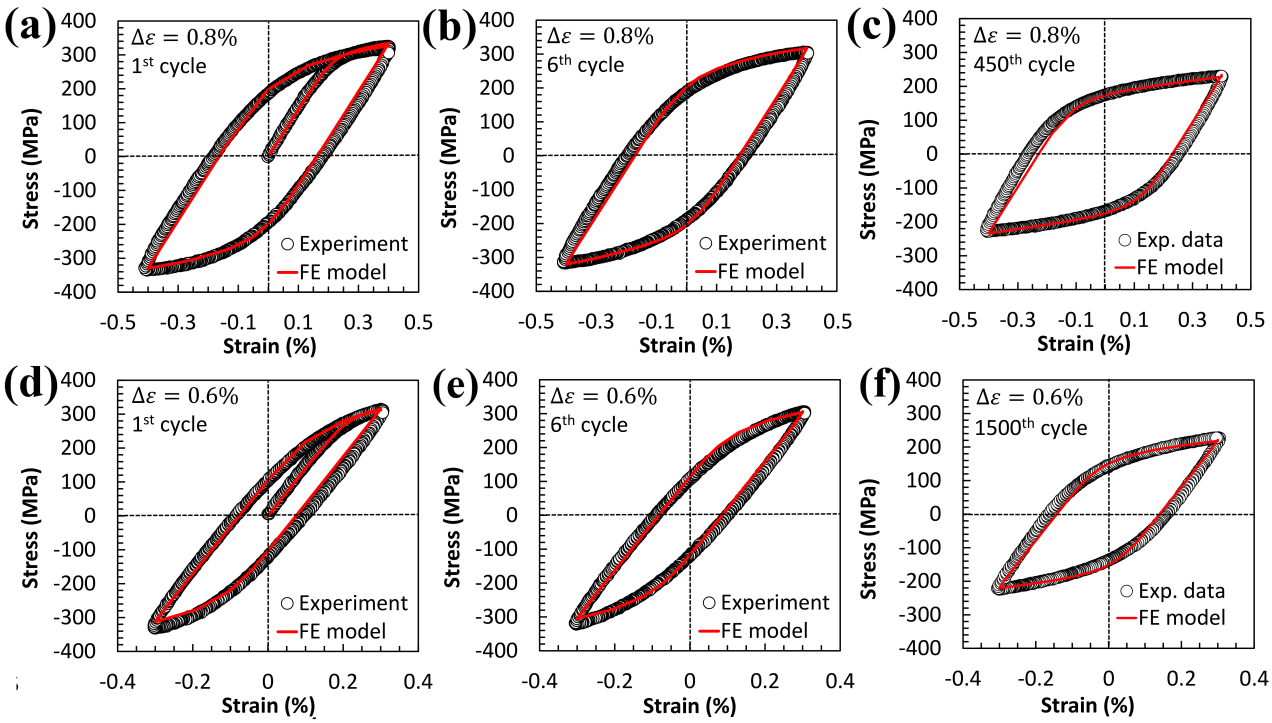

Figure 7: Simulation and measurement of stress strain response for a P91 steel with different strain ranges, in terms of (a) the first hysteresis loop, (b) the sixth hysteresis loop and (c) the half-life hysteresis loop for $\triangle\varepsilon = 0.8\%$; and (d) the first hysteresis loop, (e) the sixth hysteresis loop and (f) the half-life hysteresis loop for $\triangle\varepsilon = 0.6\%$.

strain ranges.

Figure 8 shows the localisation of stress-strain response from the polycrystal FE modelling. In Figs. 8a and b, the contour distributions of $\widetilde{\varepsilon}_p$ with $k = 1.5$ and $k = 0$, are presented, respectively. As a result of block interaction during cyclic deformation, inhomogeneous distributions can be seen in the figures for both strains. Somewhat different distribution patterns are predicted in the figures and the maximum values of the two strains occur at different sites. Therefore, the two strains lead to different predictions for the sites of crack initiation. Note here that multiple sites of 'equally' high FIP values are predicted in Figs. 8a and b. This is consistent with experimental observations of multiple micro-cracks under cyclic loading (Okamura et al., 1999). Figure 8c shows the distribution of stress triaxiality (σ_m/σ_{eq}) at the maximum stress instant in the sixth cycle. Strong heterogeneity of triaxiality can be seen with values varying from -0.2 to 1, which consequently explains the divergence between the two FIPs. Shown in Fig. 8d is the local stress-strain response in the first cycle at the critical sites with maximum $\widetilde{\varepsilon}_p$ for $k = 1.5$ and $k = 0$. The average values over the element at the critical site are used to represent the local stress and strain. Primary stress and strain components in the loading direction are presented in the figure. It can be seen in Fig. 8d that the local strain varies between approximately $\pm 1\%$, which doubles the macroscopic strain range ($\pm 0.5\%$). The maximum local stress of the first cycle is approximately 450 MPa, which is greater than the macroscopic stress (approximately 340 MPa) in the first cycle. Furthermore, though not shown, it is noted that the multiaxial stress-strain states at the critical site evolve non-proportionally.

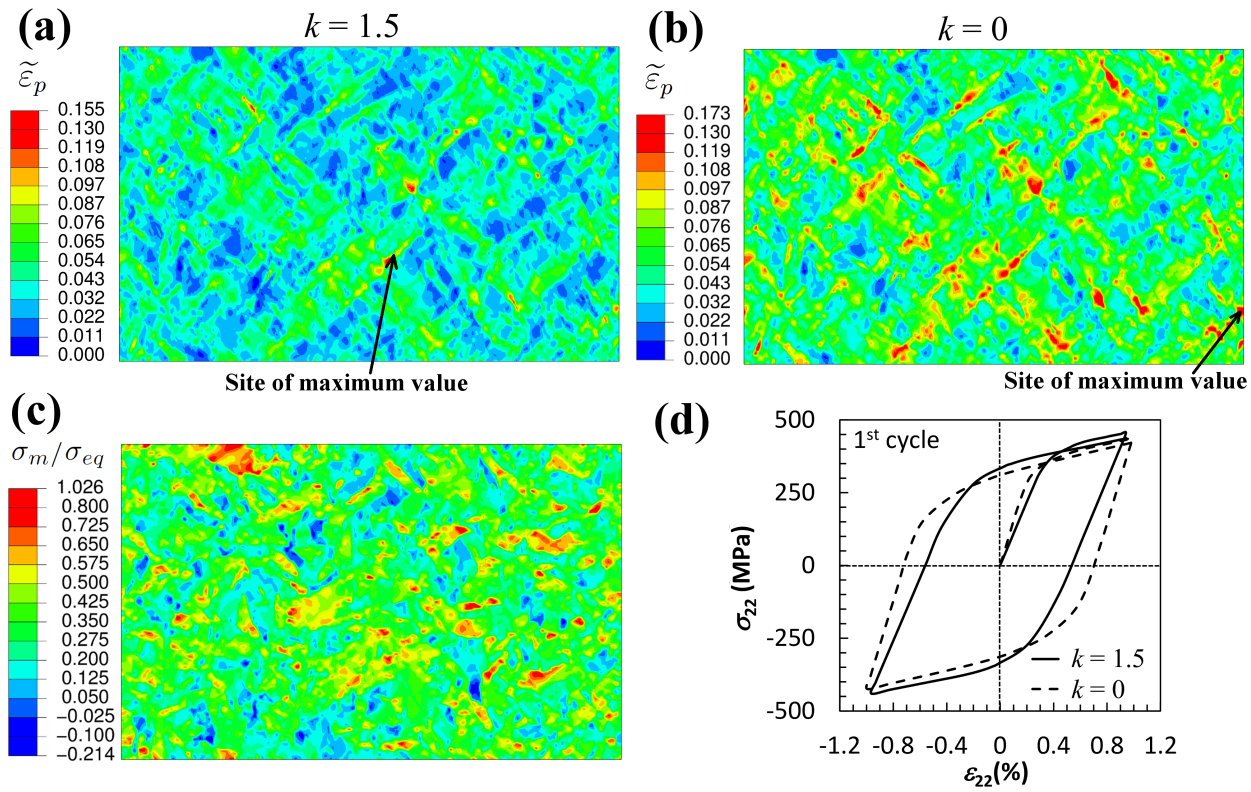

Figure 8: Simulated local stress-strain results for $\triangle\varepsilon = 1\%$ with (a) the distribution of modified plastic strain $\widetilde{\varepsilon}_p$ ($k = 1.5$) at maximum stress point in the 6^{th} cycle, (b) the distribution of plastic strain $\widetilde{\varepsilon}_p$ ($k = 0$) at maximum stress point in the 6^{th} cycle, (c) the distribution of stress triaxiality (σ_m/σ_{eq}) at maximum stress instant in the 6^{th} cycle and (d) the local stress strain response at the sites with maximum $\widetilde{\varepsilon}_p$ for $k = 1.5$ and $k = 0$.

4.2.2. Sub-grain modelling

As described earlier, the cyclic multiaxial strain histories extracted from the polycrystal FE model (e.g., Fig. 8d) have been applied to the sub-grain (lath) model (Fig. 4e) to investigate the response at the lath level. The base case is for precipitate size, $D = 130$ nm and lath thickness, $W = 0.5$ μm. As discussed by Li et al. (2014a), the initial total dislocation density ($4.2 \times 10^8 \text{mm}^{-2}$) for the lath model has been decomposed into the initial GND density (which is $3.5 \times 10^8 \text{mm}^{-2}$, corresponding to a lath misorientation angle of 2.5°) and the initial SSD density ($0.7 \times 10^8 \text{mm}^{-2}$). The mesh convergence for aggregative stress strain response has been examined in previous work (Li et al., 2014a), which presented detailed mesh convergence results for a similar sub-grain model under monotonic loading at room temperature. In order to further ensure the mesh convergence for local accumulated crystallographic slip (strain) and GND density in sub-grain modelling, we have examined four meshes for the unit cell model with total number of elements varied from approximately 1,000 to approximately 32,000 for a strain range of 1%. It is found, for the same location with peak accumulated crystallographic slip (strain), that there is only approximately 5% relative error between the mesh used and the finest mesh.

In order to validate the lath model, Figs. 9a and c show the comparison between the aggregate stress from the unit-cell lath model (solid line) and the stress at the fatigue site predicted by the polycrystal FE model (square symbols) in the first cycle for $\triangle\varepsilon = 1\%$. Figs. 9b and d show the comparisons between the two models at the half-life number of cycles. Very good agreement between the two models can be seen. In particular the kinematic hardening effect

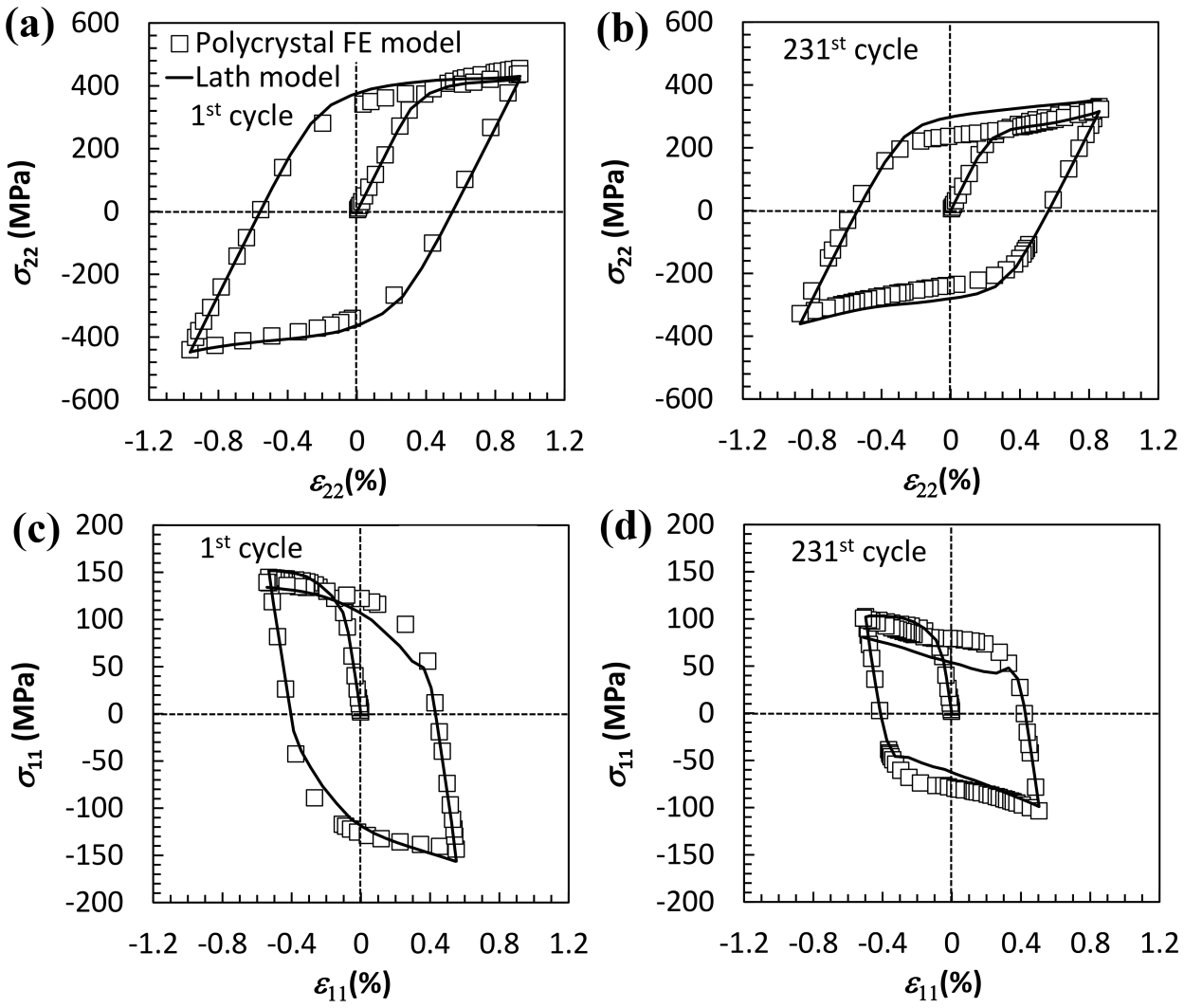

Figure 9: The cyclic stress-strain response at fatigue site using lath FE model and its comparison with the results from the polycrystal FE modelling for $\triangle\varepsilon = 1\%$ in the loading direction with (a) $N = 1$ (Fig. 8d for $k = 1.5$) and (b) half-life; and in the direction normal to the loading direction with (c) $N = 1$ and (d) half-life.

is captured by the lath model, without including the kinematic hardening term in the matrix material response. The elastic precipitates have been explicitly incorporated in the unit-cell model such that the inelastic incompatibilities between the hard precipitates and the soft matrix can be simulated and consequently lead to the kinematic hardening effect (Kassner et al., 2009).

4.3. Calibration and validation of nano-scale FIP

The lath-level contour plot of $\widetilde{\varepsilon}_p$ with $k = 1.5$ for $\triangle\varepsilon = 0.6\%$ is shown in Fig. 10. A non-symmetrical distribution can be seen as the applied strains are three-dimensional including both tension and shear. The maximum value of FIP at the lath level occurs in the matrix material as shown by the arrow in Fig. 10.

The increment in FIP per cycle at the early stage of loading is relatively constant and these averaged values are presented in Table 2. In addition, the FIP increment per cycle has also been calculated in the later (half-life) cycle analyses (discussed in Section 4.1) and these results are also provided in Table 2. Slight reductions of FIP increment are predicted at the half-life for strain ranges of 1% and 0.8%. For the strain range of 0.6%, the FIP rate is

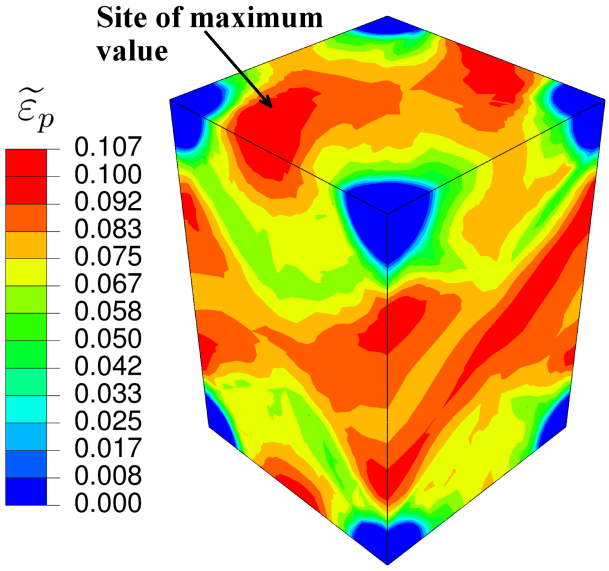

Figure 10: The distribution of $\widetilde{\varepsilon}_p$ at maximum stress point in the 6^{th} cycle for $\triangle\varepsilon = 0.6\%$.

Table 2: FIP increment per cycle at different numbers of cycles.

Strain range	$\triangle$FIP–early stage	$\triangle$FIP–half life	Half life cycle
$\triangle\varepsilon = 1.0\%$	0.0293	0.0246	231
$\triangle\varepsilon = 0.8\%$	0.0243	0.0190	450
$\triangle\varepsilon = 0.6\%$	0.0158	0.0158	1500

almost unchanged. In order to obtain the full range of FIP evolution, it is assumed, based on the results of FIP increment, that the FIP increment depends linearly on number of cycles. Therefore, after integrating the FIP increment as a linear function of number of cycles, the evolution of FIP can be obtained. The critical value of accumulated (average) crystallographic micro-slip, $\widetilde{\varepsilon}_{crit}$, is identified from comparison of the CPFE-predicted value of $\widetilde{\varepsilon}_p^{max}$, in the unit cell model, with the experimental data for $\triangle\varepsilon = 1\%$ with $N_i = 262$, leading to a critical FIP value of 7.68 for a particular precipitate and lath structure ($D = 130$ nm and $W = 0.5$ μm) and for the EBSD microstructure shown in Fig. 4b. Here, $\widetilde{\varepsilon}_{crit}$ is treated as a material constant for P91 lath matrix material.

Figure 11 shows comparison of the corresponding lath-level predictions of N_i with the estimated experimental N_i data (solid circles). N_i has been plotted against strain range using a log-log scale. As expected, the influence of EBSD microstructures (approx. 10% variation) for FCI is stronger than that for the global stress-strain response, since the local behaviour can be more sensitive to microstructure than the aggregate behaviour. Note here that two different measured EBSD microstructures are examined, to give an estimate of fatigue lifetime scatter; significantly more EBSD data is required to accurately fit probability distributions to lifetime (Koutiri et al., 2013; Charkaluk et al., 2014). In order to further validate the proposed methodology for fatigue crack initiation assessment, we have applied the present methodology to additional experiments from Barrett (2015) and Saad et al. (2011) (1% strain range) and from Okamura et al. (1999) (0.5% strain range). For the test at 0.5% strain range, the experimental result includes crack propagation life from initiation length-scale (taken here as 30 nm) to 0.3 mm, as observed. Hence, the predicted result, which does not include this propagation life, is less than the experimental, as expected. Overall, good agreement is obtained between the lath-precipitate micro-scale N_i predictions and the experiments. The

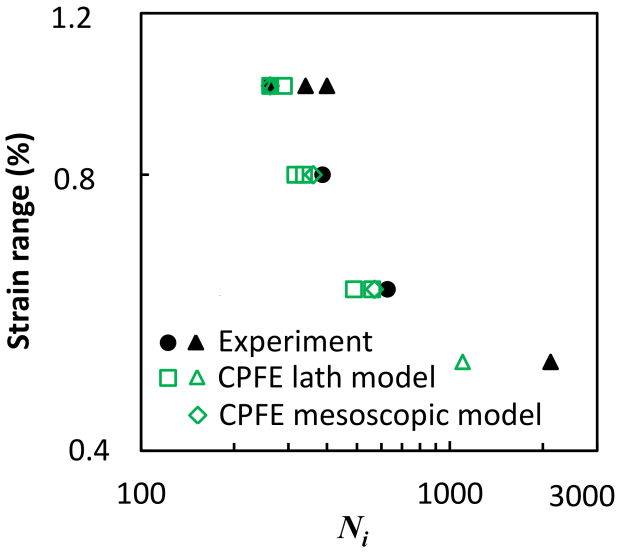

Figure 11: The comparison of FCI prediction to experimental results with $D = 130$ nm and $W = 0.5$ μm in the simulation. Here the solid circles represent the experimental data from Section 2 at a strain rate of 3.3×10^{-4}/ s, the solid triangles at the strain range of 1% are the data at a strain rate of 10^{-3}/ s (smaller life data is obtained using the method of Section 2 for the experiment of Barrett (2015) and larger one is from Saad et al. (2011) with crack of depth approximately 20 μm), the solid triangle at the strain range of 0.5% is from Okamura et al. (1999) with crack of length approximately 300 μm, the open squares represent the modelling predictions at each strain range with two EBSD structures, the open triangles are the corresponding modelling predictions using the EBSD structure of Fig. 4b.

meso-scale predictions, as in the work of Li et al. (2016), have also been included in Fig. 11 for comparison. The present CPFE lath model predictions are consistent with the meso-scale predictions; the small difference is due to the different crack initiation length-scales (the CPFE lath model predicts nano-scale initiation whereas the CPFE mesoscopic model gives micro-scale initiation).

4.4. Effects of lath and precipitate coarsening on cyclic response and FCI

Table 3: Cases of sizes of lath thickness and precipitate diameter.

	Precipitate diameter, D (nm)	Lath thickness, W (μm)
Case 1	130	0.5
Case 2	200	0.5
Case 3	130	1.0
Case 4	400	1.0

The use of the lath model allows the consideration of length-scale effects, such that the local response with regard to $M_{23}C_6$ precipitate and lath sizes can be explicitly simulated (Li et al., 2014a). In order to examine the effect of lath and precipitate coarsening on cyclic plasticity and FCI for P91 materials, three additional cases are examined with relatively large lath thickness, W, and precipitate diameter, D. Table 3 shows the sizes of lath thickness and precipitate diameter investigated here. In these simulations, the lath matrix uses the calibrated material constants and the unit-cells are subject to the same multiaxial strain histories as those obtained at the meso-scale for $D = 130$ nm and $W = 0.5$ μm. Figure 12 shows the precipitate size effects on the stress-strain hysteresis loops for different lath thicknesses. It can be seen that with increasing precipitate size the material becomes soft.

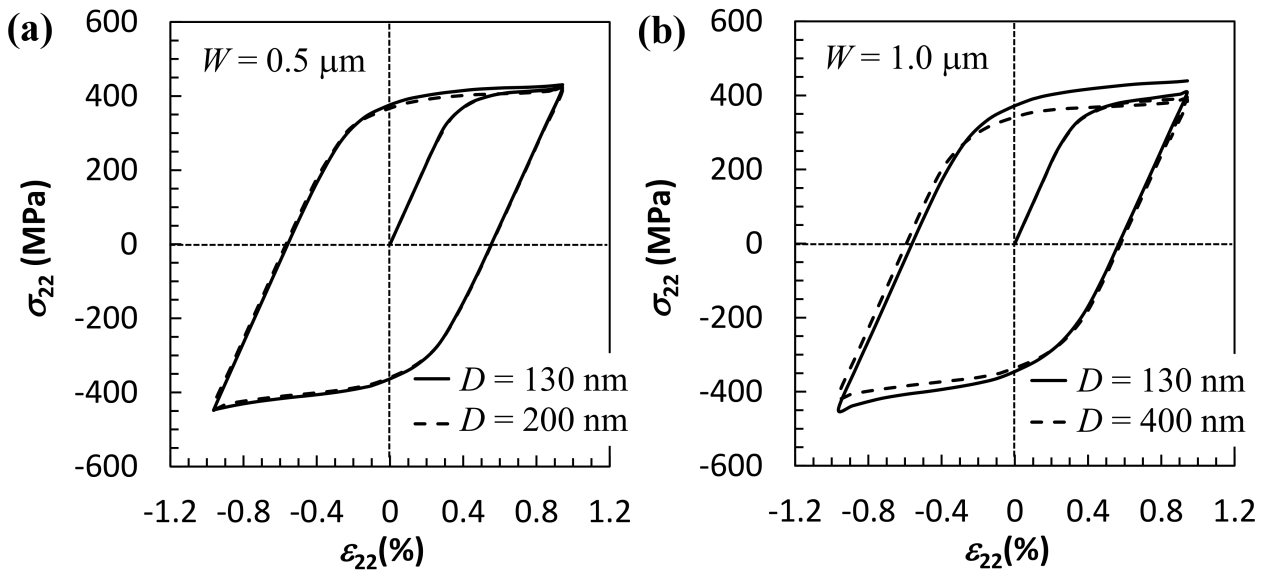

Figure 12: Effect of $M_{23}C_6$ precipitate sizes on the stress strain hysteresis loops at the fatigue site with (a) $W = 0.5$ μm and (b) $W = 1.0$ μm for $\triangle\varepsilon = 1.0\%$.

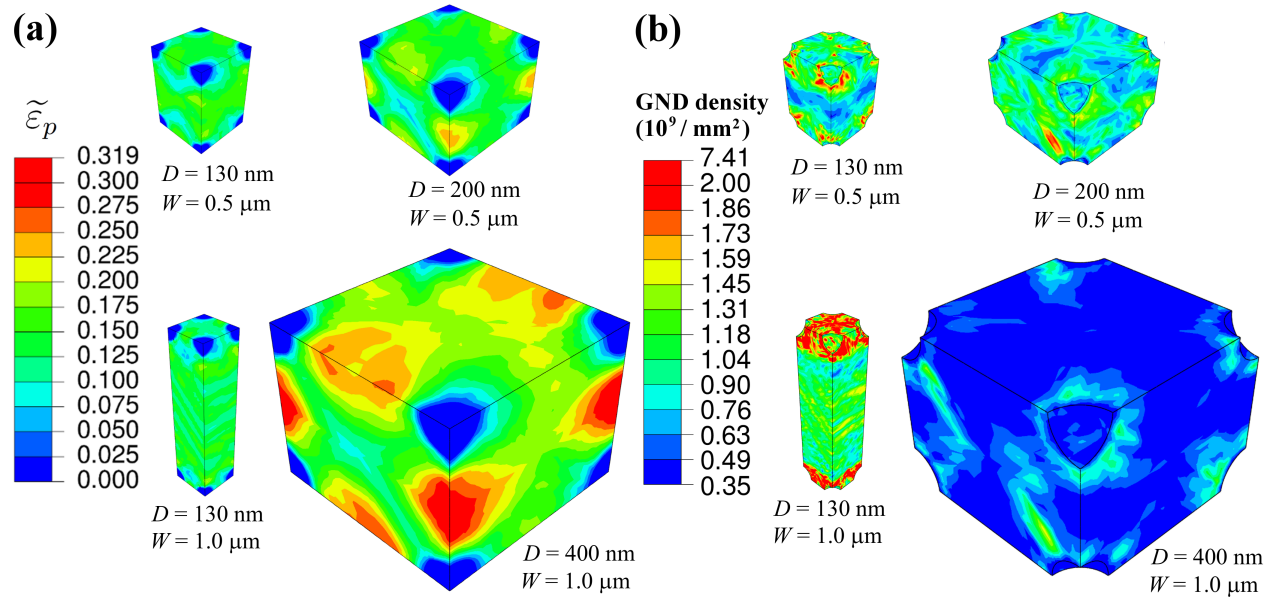

Figure 13: Effect of $M_{23}C_6$ precipitate and lath sizes on the distributions of (a) modified strain and (b) GND density at maximum stress point in the 6^{th} cycle for $\triangle\varepsilon = 1.0\%$.

The distributions of accumulated crystallographic micro-strain, $\widetilde{\varepsilon}_p$ with $k = 1.5$, for $\triangle\varepsilon = 1\%$ are shown in Fig. 13a, indicating a strong dependence on the lath and precipitate sizes. In particular, the local FIP value increases with increasing precipitate size. Figure 13b shows the contour plot of GND density at the maximum stress instant in the sixth cycle for $\triangle\varepsilon = 1.0\%$. For clarity, the precipitates in the contour plots for GND density have been removed. It should be noted that SSD density, though not shown here, is typically one order of magnitude less than GND density. In Fig. 13b, strong localised GND density can be seen in the region near precipitates which is consistent with the Orowan mechanism as discussed by Li et al. (2014a). Here, precipitates in crystals tend to bow dislocations and to be surrounded by dislocation loops after being bypassed by dislocations and consequently an increase in dislocation density,

particularly in regions near to precipitates, occurs. The significant reduction in GND density shown in Fig. 13b for the $D = 400$ nm case is simply due to the precipitate size effect and represents a key effect of precipitate coarsening, which is an important outcome of the current length-scale-dependent crystal plasticity model. The lower GND density of the $D = 400$ nm case is attributable to the lower plastic strain gradients (viz Eq. 9) for the larger precipitate size, and leads to a softer material for the coarsened case (Fig. 12b). It may be further seen in Figs. 13a and b that a qualitative correlation between accumulated crystallographic micro-strain and GND density exists such that large $\widetilde{\varepsilon}_p$ occurs at the locations with relatively low GND density and vice versa. Regions with high GND density (hence high total dislocation density) are hard to deform plastically and behave like 'elastic' material and thus lower local strains can be accumulated. Overall, the current strain gradient based modelling results indicate a strong dependence of micro-plasticity, and hence local fatigue damage, on precipitate size.

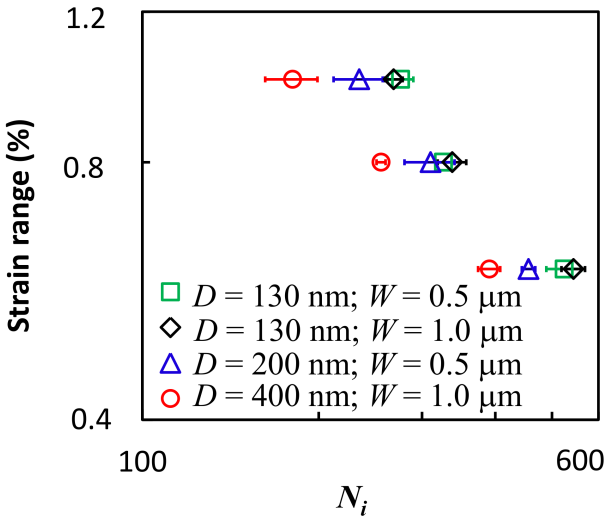

Figure 14: Simulated effects of precipitate and lath sizes on the number of cycles to FCI.

Fig. 14 shows the predicted numbers of cycles to FCI, N_i, for different sizes of lath and precipitate. It can be seen that N_i decreases with increasing D for all the strain ranges. In contrast, a relatively weak effect of increase of lath thickness, W, can be identified in Fig. 14.

5. Discussion

The primary mechanisms of softening include coarsening of microstructure (laths and precipitates), annihilation of low-angle boundary dislocations, associated decrease in dislocation density, fatigue cracking and void damage (Sauzay et al., 2005; Hu et al., 2014; Okamura et al., 1999). Annihilation of dislocations (Eqs. 7a and b) is modelled here, as demonstrated in the results of Fig. 6 due to the long-term nature of the measured softening. The effect of long-term cyclic softening has been studied in this paper through (i) modelling of different precipitate and lath sizes, the results of which are shown in Fig. 13 and (ii) evolution (reduction) of two crystal plasticity material parameters, critical shear stress and initial dislocation density based on experimental observations. A key focus of the present work is the size effect of precipitates for fatigue and the effects of precipitate coarsening due to long term exposure at high temperature.

It is well known that for general fatigue loading, stress-assisted plastic slip based fatigue criteria provide better predictions than those without stress terms, e.g., Morel and Huyen (2008) suggest a normal stress term. Here, a triaxiality term, has been introduced in the FIP, as a modulating factor on critical accumulated crystallographic slip (fatigue micro-ductility), motivated by the high temperature nature of the fatigue cracking process (e.g. the experimental observation of voids on the fracture surface) and adopting the same functional dependence on triaxiality as in macroscale ductility, also widely used for high temperature fracture (e.g., Yatomi et al., 2006). This is the justification for the exponential form of the equation, motivated originally by the void growth model of Rice and Tracey (1969). It is argued here that such an approach is valid for the so-called process zone in fatigue crack incubation at the nano-scale (e.g. at precipitate-matrix interfaces, where de-cohesion can result), initiation and early propagation, where significant plastic strain and strain gradients develop, leading to damage (e.g. nano-voids), cracking (e.g. striations) etc. The triaxiality term in Eq. (12) introduces asymmetric damage accumulation for tension and compression cycles. Therefore, to some extent, the triaxiality-dependent FIP can capture the 'applied' mean stress effect. In addition, the introduced tension-compression asymmetry shows less failure accumulation in compressive cycles than that in tensile cycles. It thus accounts for the fatigue mechanism that it is more difficult for a crack to grow during compression, due to crack surface closure. Note here that the void growth behaviour has been recently investigated theoretically and numerically through single crystal plasticity (Mbiakop et al., 2015a; Ling et al., 2016) and such approaches can provide insights into the development of more physical fatigue criteria at the nano-scale.

The fatigue criterion adopted is based on that of Manonukul and Dunne (2004), Sweeney et al. (2013) and related more recent papers (Wan et al., 2014), which present slightly modified versions, and all of which present the physics in greater detail. In those works, the crack initiation criterion is based on accumulated crystallographic slip, averaged across all slip systems, and has been shown to successfully predict both crack location (Sweeney et al., 2013) and cycles to initiation (Wan et al., 2014), within large single crystals in a four-point notch bend test specimen, compared to detailed EBSD and SEM observations. In terms of HTLCF fatigue crack initiations in P91 materials, unfortunately, due to the very small length scales of the lath-precipitate unit, coupled with the high temperatures and cyclic strain-controlled conditions, it has not yet been possible to devise an experimental methodology which allows early-stage capture of the crack nucleation phase.

The novel aspects in the present work are the proposed multiscale modelling method for simulating effect of microstructure size on cyclic micro-plasticity and FCI in P91 steels at elevated temperature, which is critical for understanding the effects of coarsening (aging) of precipitates on fatigue-creep response. It is well known that lath size and precipitate size may increase during a high temperature deformation process (e.g. Sauzay et al., 2005; Fedorova et al., 2013; Hu et al., 2014). Specifically, considerable precipitate and lath coarsening can be introduced by long term thermal and creep exposure (Fedorova et al., 2013). In reality, flexible power plants typically experience both fatigue and creep loads. Therefore, the current results in Fig. 14a suggest that the microstructure coarsening prior to fatigue (e.g., during creep) may introduce considerable detrimental effects on the fatigue response of the real components, primarily attributed to precipitate coarsening. Recently, Huang et al. (2013) have shown, through Charpy impact test, that the reduced activation ferritic martensitic steel (similar to the material examined in the current work), with $M_{23}C_6$ coarsened by heat treatment, has less absorbed energy than the material with no such coarsening. The absorbed energy in Charpy impact tests for low carbon bainite steels with different tempering temperatures has

been shown to have almost positive correlation with ductility (tensile elongation) by Li et al. (2012). Therefore, the result of Huang et al. (2013) implies that the coarsening $M_{23}C_6$ reduces material ductility. To some extent, this experimentally supports the current modelling finding.

Hu et al. (2014) have shown that during strain-controlled cyclic tests for a low activation martensitic steel at 550° C the size of $M_{23}C_6$ precipitate can increase from approximately 140 nm to approximately 180 nm due to a short term thermal exposure (less than 3 hours). The current LCF tests for P91 steels at a higher temperature of 600° C (with a thermal exposure of approximately 4 hours before FCI for $\triangle\varepsilon = 1\%$) can be expected to have more significant coarsening. From the modelling viewpoint, precipitate coarsening at the sub-grain level represents a complex physical process, which requires coupling between microstructure kinematics and nonlinear structural analysis. Recent progress has been made on simulation of microstructure evolution coupled with crystal plasticity within an FE framework (Abrivard et al., 2012), albeit for a relatively simple microstructure. Along with such a computational multi-physics method, therefore, the present multiscale modelling framework could even more accurately quantify the effects of microstructural evolution on fatigue behaviour in P91 steels.

Besides microstructure evolution during component lifetime, there is spatial microstructural heterogeneity for the relevant power plant components, such as P91 weldments, which are typically the locations of premature failure during service. The present work has demonstrated the predictive capability of a strain-gradient based crystal plasticity model for cyclic behaviour and fatigue of P91 steels, in particular with respect to lath and precipitate sizes. Future work, therefore,aims to examine the cyclic plasticity and fatigue cracking of P91 weldments with size gradients of block, lath and precipitates.

6. Concluding remarks

The main results and findings are as follows,

1. A multiscale, strain-gradient, crystal plasticity modelling methodology is developed to investigate cyclic plasticity and fatigue in a P91 tempered martensite ferritic steel at elevated temperature, with microstructural details at both grain and sub-grain levels explicitly considered. The modelling hysteresis stress-strain loops are in good agreement with experiments. It is further found that the $M_{23}C_6$ precipitates primarily introduce kinematic hardening to P91 steels.
2. A nano-scale fatigue indicator parameter based on accumulated crystallographic slip (strain), modulated by triaxiality, to incorporate load amplitude effects, is implemented in the multiscale methodology to predict the fatigue crack initiation both spatially and cyclically. The predictions agree well with experiments.
3. The multiscale and length-scale-dependent modelling results indicate a strong dependence of cyclic micro-plasticity and fatigue on the precipitate and lath sizes. The coarsening of $M_{23}C_6$ precipitates at elevated temperature was shown to have a detrimental effect on the cyclic response and low cycle fatigue life of P91 steels.

Acknowledgment

This publication has emanated from research conducted with the financial support of Science Foundation Ireland under grant numbers SFI/10/IN.1/I3015 and SFI/14/1A/2604. The modelling work was supported by the Irish Center for High-End Computing (ICHEC). Helpful discussions with Dr. Peter Tiernan, Mr. Brian Golden and Dr. Yina Guo of the Materials and Surface Science Institute (MSSI) at University of Limerick, Ireland; Ms. Eimear

O'Hara of National University of Ireland, Galway; and Mr. Stephen Scully of Electricity Supply Boad (ESB International), Ireland are gratefully acknowledged.

Appendix. Derivation of maximum cyclic stress as a function of number of cycles

It should be noted that the method in this section is simply intended to provide experimental estimates of N_i for comparison with the results of CPFE methodology of Section 3 significantly more physically-based.

For a fully reversed strain-controlled cyclic test, the maximum stress in each cycle is given by

$$\sigma_{\max}(N) = E\left[\frac{\triangle\varepsilon}{2} - \frac{\triangle\varepsilon_p(N)}{2}\right], \tag{A-1}$$

where N is the cycle number, E is the macroscopic Young's modulus and $\triangle\varepsilon$ and $\triangle\varepsilon_p(N)$ are the total (applied) strain range and plastic strain range, respectively. Note that for a strain-controlled test, $\triangle\varepsilon$, is constant. A modified Taylor relationship (Taylor, 1934) can be used to describe the maximum stress in terms of dislocation density, ρ,

$$\sigma_{\max} = \sigma_0 + \alpha G b\sqrt{\rho}, \tag{A-2}$$

where σ_0 is a constant, α is a statistical coefficient and G is the macroscopic shear modulus.

The evolution of total dislocation density is given as follows (Mecking and Kocks, 1981)

$$d\rho = (k_g\sqrt{\rho} - d_a\rho)\, dp, \tag{A-3}$$

where p is the macroscopic accumulated plastic strain, k_g and d_a are the accumulation and annihilation coefficients for the material. Under cyclic loading, dp is defined as:

$$dp = 2\triangle\varepsilon_p dN. \tag{A-4}$$

From Eq. (A-1), the increment in maximum stress per cycle, $d\sigma_{\max}$ is given by

$$d\sigma_{\max} = -\frac{E}{2} d\triangle\varepsilon_p. \tag{A-5}$$

Taking the differential of both sides of Eq. (A-2) leads to

$$d\sigma_{\max} = \frac{\alpha G b}{2\sqrt{\rho}} d\rho, \tag{A-6}$$

Combining Eqs. (A-5) and (A-6) results in a differential equation in terms of plastic strain and dislocation density,

$$\frac{E}{2} d\triangle\varepsilon_p + \frac{\alpha G b}{2\sqrt{\rho}} d\rho = 0. \tag{A-7}$$

Substituting, Eq. (A-4) into Eq. (A-3) and subsequently into Eq. (A-7) leads to

$$\frac{E}{2} d\triangle\varepsilon_p + \alpha G b\,(k_g - d_a\sqrt{\rho})\,\triangle\varepsilon_p dN = 0. \tag{A-8}$$

From Eq. (A-1) and Eq. (A-2),

$$\sqrt{\rho} = \frac{E}{2\alpha G b}\left(\triangle\varepsilon - \frac{2\sigma_0}{E} - \triangle\varepsilon_p\right). \tag{A-9}$$

Substituting Eq. (A-9) into Eq. (A-8) leads to a differential equation for $\triangle\varepsilon_p$ as a function of number of cycles N for a polycrystal

$$d\triangle\varepsilon_p + \left(k_1 + k_2\triangle\varepsilon_p\right)\triangle\varepsilon_p dN = 0, \tag{A-10}$$

where k_1 and k_2 are material constants,

$$k_1 = \frac{2\alpha G b}{E}k_g - d_a\left(\triangle\varepsilon - \frac{2\sigma_0}{E}\right), \tag{A-11a}$$

$$k_2 = d_a. \tag{A-11b}$$

After integrating Eq. (A-10), the theoretical expression for the plastic strain range, $\triangle\varepsilon_p$, can be obtained as follows

$$\triangle\varepsilon_p\left(N\right) = p'\left(1\right)\left[\frac{k_1}{\left(2k_1 + p'\left(1\right)k_2\right)e^{k_1(N-1)} - p'\left(1\right)k_2}\right], \tag{A-12}$$

where $p'\left(1\right)$ is the value of dp/dN when $N = 1$. To achieve a good approximation, $p'\left(1\right) = p\left(1\right)$ and may be obtained from the data in the first cycle as, $p\left(1\right) = 2\triangle\varepsilon - 4\sigma_{\max}\left(1\right)/E$. Substituting Eq. (A-12) into Eq. (A-1), an expression for the maximum stress as a function of cycle number, N, is obtained as follows

$$\sigma_{\max}\left(N\right) = \frac{E}{2}\left[\triangle\varepsilon - \frac{p\left(1\right)k_1}{\left(2k_1 + p\left(1\right)k_2\right)e^{k_1(N-1)} - p\left(1\right)k_2}\right]. \tag{A-13}$$

Equation (A-13) is applicable only when $N \leqslant N_i$ and the constants k_1 and k_2 are determined by fitting to the experimental data (Fig. 2).

References

ABAQUS V6.11, 2011. Hibbitt, Karlsson and Sorensen Inc., Providence, RI, USA.

Abrivard, G., Busso, E.P., Forest, S., Appolaire, B., 2012a. Phase field modelling of grain boundary motion driven by curvature and stored energy gradients. part I: theory and numerical implementation. Philos. Mag. 92(28-30), 3618–3642.

Ali, D., Mushtaq, N., Butt, M.Z., 2011. Investigation of active slip-systems in some body-cnetered cubic metals. J Mater Sci 46:3812-3821.

Anahid, M., Samal, M.K., Ghosh, S., 2011. Dwell fatigue crack nucleation model based on using crystal plasticity finite element simulations of polycrystalline Titanium alloys. J. Mech. Phys. Solids 59, 2157–2176.

Barrett RA, 2015. Experimental Characterisation and Computational Modelling of High Temperature Degradation of 9Cr Steels Including Microstructural Effects. PhD Thesis, Mechanical Engineering, NUI Galway, Ireland.

Brünig, M., Gerke, S., Hagenbrock, V., 2013. Micro-mechanical studies on the effect of the stress triaxiality and the Lode parameter on ductile damage. Int. J. Plast. 50, 49–65.

Busso, E.P., McClintock, F.A., 1996. A dislocation mechanics-based crystallographic model of a B2-type intermetallic alloy. Int. J. Plast. 12(1), 1–28.

Busso, E.P., Meissonnier, F.T., O'Dowd, N.P., 2000. Gradient-dependent visco-plastic deformation of two-phase single crystals. J. Mech. Phys. Solids 48, 2333–2361.

Charkaluk, E., Constantinescu, A., Szmytka, F., Tabibian, S., 2014. Probability density functions: From porosities to fatigue lifetime, Int J Fatigue, 63, 127-136.

Cheong, K.S., Busso, E.P., 2004. Discrete dislocation density modelling of single crystal fcc polycrystals. Acta Mater. 52, 5665–5675.

Cheong, K.S., Busso, E.P., 2006. Effects of lattice misorientations on strain heterogeneities in fcc polycrystals. J. Mech. Phys. Solids 54, 671–689.

Dang Van K, Macro-micro approach in high-cycle multiaxial fatigue. In Advances in Multiaxial Fatigue. edited by McDowell DL, and Ellis R. American Society for Testing and Materials STP 1191. Philadelphia 1993,120–130.

Dang Van K, Papadopoulos IV. Multiaxial fatigue failure criterion: a new approach. Fatigue 87: Proc. Third Int. Conf. on Fatigue and Fatigue Thresholds, EMAS Warley, UK, 1987. 997-1008.

Dunne, F.P.E., 2014. Fatigue crack nucleation: Mechanistic modelling across the length scales. Curr. Opin. Solid State Mater. Sci. 18, 170–179.

Dunne, F.P.E., Kiwanuka, R., Wilkinson, A.J., 2012. Crystal plasticity analysis of micro-deformation, lattice rotation and geometrically necessary dislocation density. Proc. R. Soc. A 468(2145), 2509–2531.

Dunne, F.P.E., Wilkinson, A.J., Allen, R., 2007. Experimental and computational studies of low cycle fatigue crack nucleation in a polycrystal. Int. J. Plast. 23, 273–295.

Essmann, U., Mughrabi, H., 1979. Annihilation of dislocations during tensile and cyclic deformation and limits of dislocation density. Philosophical Magazine A 40, 731-756.

Farragher, T.P., 2014. Thermomechanical Analysis of P91 Power Plant Components. PhD Thesis, Mechanical Engineering, NUI Galway, Ireland.

Fedorova, I., Kipelova, A., Belyakov, A., Kaibyshev, R., 2013. Microstructure evolution in an advanced 9 pct Cr martensitic steel during creep at 923 K (650° C). Metall. Mater. Trans. A 44A, S128–S135.

Franciosi, P., Le, L.T., Monnet, G., Kahloun, C., Chavanne, M.H., 2015. Investigation of slip system activity in iron at room temperature by SEM and AFM in-situ tensile and compression tests of iron single crystals. Int J Plast 65, 226–249.

Giroux, P.F., Experimental study and simulation of cyclic softening of tempered martensite ferritic steels [Ph.D. thesis]. l'Ecole Nationale Superieure des Mines de Paris; 2011.

Grogan, D.M., Bradaigh, C.M.O., McGarry, J.P., Leen, S.B., 2015. Damage and permeability in tape-laid thermoplastic composite cryogenic tanks. Composites Part A 78,390-402.

Golden, B., Li, D.F., Tiernan, P., Scully, S., O'Dowd, N., 2015. Deformation characteristics of a high-chromium, power plant steel at elevated temperatures. Proceedings of 2015 ASME Pressure Vessels and Piping Division Conference, July 2015, Boston, USA.

Golden, B.J., Li, D.F., Guo, Y.N., Tiernan, P., Leen, S.B., O'Dowd, N.P., 2016. Microscale deformation of a tempered martensite ferritic steel: Modelling and experimental study of grain and sub-grain interactions. J. Mech. Phys. Solids 86, 42–52.

Hochhalter, J.D., Littlewood, D.J., Veilleux, M.G., Bozek, J.E., Maniatty, A.M., Rollett, A.D., Ingraffea, A.R. 2011. Modelling and Simulation in Materials Science and Engineering 19(3), 035008.

Hu, X., Huang, L., Yan, W., Wang, W., Sha, W., Shan, Y., Yang, K., 2014. Low cycle fatigue properties of CLAM steel at 823 K. Mater. Sci. Eng. A 613, 404–413.

Huang, L., Hu, X., Yang, C., Yan, W., Xiao, F., Shan, Y., Yang, K., 2013. Influence of thermal aging on microstructure and mechanical properties of CLAM steel. J. Nucl. Mater. 443, 479–483.

Kassner, M.E., Geantil, P., Levine, L.E., Larson, B.C., 2009. Backstress, the Bauschinger effect and cyclic defor mation. Mater. Sci. Forum 604-605, 39–51.

Kiran, R., Khandelwal, K., 2015. A micromechanical cyclic void growth model for ultra-low cycle fatigue. Int. J. Fatigue 70, 24–37.

Koutiri, I., Bellett, D., Morel, F., Pessard, E., 2013. A probabilistic model for the high cycle fatigue behaviour of cast aluminium alloys subject to complex loads. Int J Fatigue, 47, 137–147.

Kuwamura, H., 1997. Transtion between fatigue and ductile fracture in steel. J Struct Eng 123(7): 864–870.

Lee, J.S., Maruyama, K., 2015. Mechanism of microstructural deterioration preceding type IV failure in weldment of mod. 9Cr-1Mo steel. Met Mater Int 21(4), 639–645.

LE, V.D., Morel, F., Bellett, D., Pessard, E., Saintier, N., Osmond, P., 2015. Microstructural-based Analysis and Modelling of the Fatigue Behaviour of Cast Al-Si Alloys. Procedia Eng, 133, 562–575.

Li, D., Huang F., Wang, S., Xiong, Y., Xing, S., Xiong, T., 2012. Effect of tempering temperature on microstructures and properties of niobium and titanium microalloying low carbon bainite steel. 2^{nd} International Conference on Electronic & Mechanical Engineering and Information Technology, September 2012, Shenyang, Liaoning, China.

Li, D.F., O'Dowd, N.P., 2011. On the evolution of lattice deformation in austenitic stainless steels–The role of work hardening at finite strains. J. Mech. Phys. Solids 59, 2421–2441.

Li, D.F., Golden, B.J., O'Dowd, N.P., 2014a. Multiscale modelling of mechanical response in a martensitic

steel: A micromechanical and length-scale-dependent framework for precipitate hardening. Acta Mater. 80, 445–456.
Li, D.F., Golden, B.J., Zhang, S.Y., Davydov, V., Tiernan, P., O'Dowd, N.P., 2014b. The role of plasticity in the transverse lattice strain evolution of a martensitic steel. Metall. Mater. Trans. A 45A, 5829–5833.
Li, D.F., Barrett, R.A., O'Donoghue, P.E., Hyde, C., O'Dowd, N.P., Leen, S.B. 2016. Micromechanical finite element modelling of thermo-mechanical fatigue for P91 steels. Int J Fatigue. 87, 192-202.
Ling, C., Besson, J., Forest, S., Tanguy, B., Latourte, F., Bosso, E., 2016. An elastoviscoplastic model for porous single crystals at finite strains and its assessment based on unit cell simulations. Int J Plast, 84, 58–87.
Maitournam, M.H., Krebs, C., Galtier, A., 2011. A multiscale fatigue life model for complex cyclic multiaxial loading. Int J Fatigue, 33(2),232–240.
Manonukul, A., Dunne, F.P.E., 2004. High and low cycle fatigue crack initiation using polycrystal plasticity. Proc R Soc London 460(2047):1881–1903.
Marichal, C., Van Swygenhoven, H., Van Petegem, S., Borca, C., 2013. {110} slip with {112} slip traces in bcc tungsten. Sci Rep 3:2547.
Mbiakop, A., Constantinescu, A., Danas, K., 2015. An analytical model for porous single crystals with ellipsoidal voids. J Mech Phys Solids, 84, 436–467.
Mbiakop, A., Constantinescu, A., Danas, K., 2015. On void shape effects of periodic elasto-plastic materials subjected to cyclic loading. Eur J Mech A Solids, 49, 481–499.
McDowell, D.L., Dunne, F.P.E., 2010. Microstructure-sensitive computational modeling of fatigue crack formation. Int. J. Fatigue 32, 1521–1542.
Mecking, H., Kocks, U.F., 1981. Kinetics of flow and strain hardening. Acta Metall. 29(11), 1865–1875.
Morel, F., Huyen, N., 2008. Plasticity and damage heterogeneity in fatigue, Theor Appl Fract Mech, 49(1), 98–127.
Mughrabi, H., 2013. Cyclic slip irreversibility and fatigue life: A microstructure-based analysis. Acta Mater 61, 1197–1203.
Okamura, H., Ohtani, R., Saito, K., Kimura, K., Ishii, R., Fujiyama, K., Hongo, S., Iseki, T., Uchida, H., 1999. Basic investigation for life assessment technology of modified 9Cr-1Mo steel. Nucl. Eng. Des. 193, 243–254.
Orowan, E., Symposium on internal stress. In: Metals and alloys. London: Institute of Metals; 1948.
Pessard, E., Morel, F., Bellett, D., Morel, A., 2012. A new approach to model the fatigue anisotropy due to non-metallic inclusions in forged steels. Int J Fatigue, 41, 168–178.
Razumovskiy, V.I., Ruban, A.V., Korzhavyi, P.A., 2011. Effect of temperature on the elastic anisotropy of pure Fe and Fe0.9Cr0.1 random alloy. Phys. Rev. Lett. 107, 205504.
Rice, J.R., Tracey, D., 1969. On the ductile enlargement of voids in triaxial stress fields. J. Mech. Phys. Solids 17(3), 201–217.
Rosien, F.J. and Ostertag, C.P., 2009. Low cycle fatigue behaviour of constraint connections. Mater Struct 42: 161-170.
Roters, F., Eisenlohr, P., Hantcherli, L., Tjahjanto, D.D., Bieler, T.R., Raabe, D., 2010. Overview of constitutive laws, kinematics, homogenization and multiscale methods in crystal plasticity finite-element modeling: Theory, experiments, applications. Acta Mater. 58, 1152–1211.
Saad AA, Sun W, Hyde TH, Tanner DWJ. Cyclic softening behaviour of a P91 steel under low cycle fatigue at high temperature. Procedia Eng. 2011;10:1103–08.
Sangid, M.D., 2013. The physics of fatigue crack initiation. Int. J. Fatigue 57, 58–72.
Sauzay, M., Brillet, H., Monnet, I., Mottot, M., Barcelo, F., Fournier, B., Pineau, A., 2005. Cyclically induced softening due to low-angle boundary annihilation in a martensitic steel. Mater. Sci. Eng. A 400-401, 241–244.
Sauzay, M., Fournier, B., Monnet, I., Mottot, M., Pineau, A., 2008. Cyclic softening of martensitic steels at high temperature–experiments and physically based modelling. Mater. Sci. Eng. A 483-484, 410–414.
Sawada, K., Kushima, H., Tabuchi, M., Kimura, K., 2011. Microstructural degradation of Gr.91 steel during creep under low stress. Mater. Sci. Eng. A 528, 5511–5518.
Signor, L., Villechaise, P., Ghidossi, T., Lacoste, E., Gueguen, M., Courtin, S., 2016. Influence of local crystallographic configuration on microcrack initiation in fatigued 316LN stainless steel: Experiments and crystal plasticity finite elements simulations, Mater Sci Eng A, 649, 239–249.
Sines G, Behaviour of metals under complex stresses. In: Sines G, Waisman JL, eds., Metal Fatigue, New York: McGraw-Hill, 1959, 145–169.
Srinivas Prasad, B.S., Rajkumar, V.B., Hari Kumar, K.C., 2012. Numerical simulation of precipitate evolution in ferritic martensitic power plant steels. CALPHAD 36, 1–7.
Sweeney, C.A., O'Brien, B., Dunne, F.P.E., McHugh, P.E., Leen, S.B., 2014. Strain-gradient modelling of

grain size effects on fatigue of CoCr alloy. Acta Mater. 78, 341–353.
Sweeney, C.A., Vorster, W., Leen, S.B., Sakurada, E., McHugh, P.E., Dunne, F.P.E., 2013. The role of elastic anisotropy, length scale and crystallographic slip in fatigue crack nucleation. J. Mech. Phys. Solids 61, 1224-1240.
Suresh, S. Fatigue of Materials. 1998 Cambridge University Press.
Taylor, G.I., 1934. The mechanism of plastic deformation of crystals. Part I. Theoretical. Proc. Roy. Soc. Lond. A145, 362–387.
Terzi, S., Salvo, L., Sury, M., Limodin, N., Adrien, J., Maire, E., Pannier, Y., Bornert, M., Bernard, D., Felberbaum, M., Rappaz, M., Bolle, E., 2009. In situ X-ray tomography observation of inhomogeneous deformation in semi-solid aluminium alloys. Scripta Mater, 61(5), 449-452.
Trattnig, G., Antretter, T., Pippan, R., 2008. Fracture of austenitic steel subject to a wide range of stress triaxiality ratios and crack deformation modes. Eng. Fract. Mech. 75, 223–235.
Yatomi, M., O'Dowd, N.P., Nikbin, K.M., Webster, G.A. 2006. Theoretical and numerical modelling of creep crack growth in a carbon manganese steel. Eng Fract Mech 73, 1158–1175.
Wan, V.V.C., MacLachlan, D.W., Dunne, F.P.E., 2014. A Stored energy criterion for fatigue crack nucleation in polycrystals. Int J Fatigue 68, 90-102.
Wang, L., Li, M., Almer, J., 2014. Investigation of deformation and microstructural evolution in Grade 91 ferritic-martensitic steel by in situ high-energy X-rays. Acta Mater 62, 239–249.